INTERIM REPORT

Isolating and Discriminating Overlapping Signatures in Cluttered Environments

SERDP Project MR-1664

MAY 2011

Ben Barrowes
Fridon Shubitidze
U.S. Army Corps of Engineers Research and Development Center

SERDP
DOD ▪ EPA ▪ DOE

Isolating and Discriminating Overlapping Signatures in Cluttered Environments

MR-1664

Interim Report

Submitted to

Strategic Environmental Research and Development Program (SERDP)

May 11, 2011

Revision **2.0**

By

U.S. Army Corps of Engineers Research and Development Center
Cold Regions Research and Engineering Laboratory (CRREL)
72 Lyme Road
Hanover, NH 03755

Principal Investigators

Drs. Ben Barrowes and Fridon Shubitidze
benjamin.e.barrowes@usace.army.mil

Contents

1 Abstract

SERDP project MR-1664 entitled "Isolating and Discriminating Overlapping Signatures in Cluttered Environments" is approximately halfway complete. Significant progress has been made in working toward the original objectives of the project. Three new methods for localizing multiple sources in close proximity using EMI data have been developed and tested. Specifically, these methods are:

- A multiple dipole search method based on a gradient search algorithm utilizing an analytical Jacobian (see Sec. 4.2)
- A combined Joint Diagonalization (JD) and Orthonormalized Volume Magnetic Source (ONVMS) method (see Sec. 4.3)
- Source localization based MUSIC algorithm applied to EMI data (see [1])

Canonical targets of various shapes, sizes and material parameters have been fabricated (see Sec. 4.1. Data acquired from these targets as well as standard UXO targets has been acquired by the TEMTADS and MPV2 instruments in many multitarget configurations (see Sec. 4.1). The methods developed to date under this MR-1664 have been able to isolate and discriminate up to six targets simultaneously in the case of lab data (see Sec. 5). The JD method is able to almost instantaneously provide a good estimate for the number of distinct targets in the EMI data. After this estimate is obtained, the first or second methods delineated above (and described below) are used to invert for the parameters of the N identified targets.

List of Acronyms (and page references to first use)

BOR	Body of Revolution – first used on page (15)
CRREL	Cold Regions Research and Engineering Lab – first used on page (1)
EM	Expectation Maximization – first used on page (1)
EMI	Electromagnetic Induction – first used on page (ii)
ERDC	Engineering Research and Development Center – first used on page (1)
JD	Joint Diagonalization – first used on page (ii)
MEC	Munitions and Explosives of Concern – first used on page (2)
MM	Munitions Management – first used on page (ii)
MPV2	Man-Portable Vector Sensor, Version 2.0 – first used on page (ii)
MQS	magnetoquasistatic – first used on page (47)
MR	Munitions Response – first used on page (ii)
NRL	Naval Research Laboratory – first used on page (32)
NSMS	Normalized Surface Magnetic Source – first used on page (1)
ONVMS	Orthonormalized Volume Magnetic Source – first used on page (ii)
SEA	Standardized Excitations Approach – first used on page (1)
SERDP	Strategic Environmental Research and Development Program – first used on page (ii)
SVM	Support Vector Machines – first used on page (1)
TEMTADS	Time-domain Electromagnetic Multi-sensor Tower Array Detection System – first used on page (ii)
USACE	United States Army Corps of Engineers – first used on page (1)
UXO	UneXploded Ordnance – first used on page (ii)

Keywords: electromagnetic induction, multiple targets, rigorous models, inversion, dipole model, joint diagonalization, ONVMS

Acknowledgements: This project was funded by the Strategic Environmental Research and Development Program (SERDP) under project MR-1664. Drs. Jeff Marqusee, Anne Andrews, Herb Nelson, and the review committee for SERDP, provided support and constructive reviews during the course of the project.

List of Figures

List of Tables

2 Objectives

The objectives of the proposed work are to mitigate the effects of discrete metallic clutter from EMI data, and the simultaneous discrimination of multiple anomalies in close proximity with overlapping EMI responses. Specifically, we aim to develop a robust approach for processing high quality data from next generation EMI instruments to mitigate the effects of clutter by isolating their EMI signatures after locating them individually, and then discriminate UXO from non-UXO targets at highly contaminated sites that include challenging terrain, vegetation, and geology using rigorous models that may include interaction effects.

1. Develop an N-target estimator, able to provide estimates of the number of targets present in the sensors field of view along with their locations and orientations, without resorting to computationally expensive optimizations. This locator will utilize high quality EMI data without solving the traditional ill-posed inverse scattering problem.

   Here, two approaches for this N-target locator will be reported (Sec. 4):

   (a) A multiple dipole search method based on a gradient search algorithm utilizing an analytical Jacobian (see Sec. 4.2)

   (b) A combined Joint Diagonalization (JD) and Orthonormalized Volume Magnetic Source (ONVMS) method (see Sec. 4.3)

   (c) Source localization based MUSIC algorithm applied to EMI data (not reported here, see [1])

2. Formulate robust classifiers that segregate N targets into UXO and non-UXO. This classifier will consider model based parameters such as volume estimates and HAP estimate of polarizability and may be based on rapid statistical techniques such as Support Vector Machines (SVM).

   Significant progress on this has been made. For example, our group recently achieved a very encouraging score (no false negatives and very few false positives) on our dig list for the Camp Butner demonstration site using an Expectation Maximization (EM) algorithm (see [2]).

3. Discriminate UXO-like targets using rigorous (NSMS, SEA) models which explicitly include coupling between targets if required (see Sec. 4.2–Sec. 4.3).

Unmatched high quality data from advanced instruments in the time domain will be used (Sec. 4.1). These instruments, specifically in this report the TEM-TADS and MPV2 instruments, provide tremendous data diversity including vector data, monostatic and multistatic measurements, allowing us to assess the benefits of data diversity. As well, rigorous, physically complete models (see Sec. 4.2–Sec. 4.3) are being developed to discriminate targets and anomalies based on their extracted EMI model parameters. These high fidelity models reduce to dipole models but can also provide much more information than traditional dipole models alone. The JD method, for example, trades knowledge of the target's **position** and what the **amplitude** of its polarizabilities are for a rapid determination of the **shape** of those polarizabilities.

3 Background

EMI data acquired over subsurface anomalies must be processed and inverted in order to discriminate innocuous scrap metal or geology from munitions and explosives of concern (MEC). At highly contaminated sites, processing data containing responses from disperse metallic clutter and overlapping anomalies is a difficult task both theoretically and computationally. Response from shallow yet small metallic clutter can often obscure deeper targets of interest (for example, see Figs. 28–30), and the electromagnetic induction (EMI) response from targets in close proximity may affect each other due to mutual coupling [3, 4] and confuse or confound inversion schemes. These realities often lead to misclassification at best, or a complete failure of the routine at worst. Both outcomes raise the probability of false alarm and the probability of a missed MEC.

Prior approaches aimed at addressing the topic of discriminating multiple overlapping signals have serious limitations. Some studies cast the problem as a blind source separation (BSS) problem [5–7]. These studies assumed no interaction between anomalies which interaction is known to exist [8], were constrained to a maximum of two targets [5], were simulations that had prior knowledge of the target [6], or a combination of similar limitations. Other studies used data from multiple instruments (such as simultaneous EMI and GPR) which can be costly and is not generally available [9–12]. ESTCP project UX-0415 attempted to use a pair of dipoles to accommodate 2 targets and an iterative approach for isolating multiple dipole sources. However other work [13] has shown that even single multi-part UXO's require multiple dipoles for effective representation, and an optimization

may not be able to distinguish a single heterogeneous UXO from multiple UXOs.

A recent SERDP project, MM-1637, *Selecting Optimal Models for Inverting EMI Data* concentrates on model selection and data quality to determine whether a given data set should be modeled as one or two targets. They then use a probability based inversion scheme to invert the data based on their assumed number of targets. Our approach differs from these approaches in fundamental ways. First, we are using analytical techniques to mitigate the noise due to disperse clutter which problem MM-1637 does not address. Second, we are developing methods to locate N targets simultaneously as a initial step either prior to or during inversion (Sec. 4) whereas MM-1637 only addresses the cases of one or two objects. This N-target locator (the JD method (see Sec. 4.3) and MUSIC target localizer [1] avoid time consuming and computationally complex inversion stages that MM-1637 does not avoid. Finally, we have access to the latest generation, well located instruments which provide high quality data from realistic field conditions.

In these studies, the objects are generally modeled using simple dipole models to accommodate two targets and the targets are isolated via a laborious time consuming inversion approach. Problems during the inversion phase also arise when the digital geophysical data are very low quality and simple phenomenological models fail to accurately represent overlapping EMI signals from anomalies in close proximity. In addition, many single heterogeneous targets may be well modeled by two dipoles, further complicating inversion processes based solely on dipoles. In these cases, the parameters of the phenomenological model (which are used as discrimination features in statistical decisions algorithms) become unseparable and as a result the classification is unreliable. Our approach detailed in Sec. 4.2 uses multiple dipoles seeded into the subsurface space, but uses the analytical Jacobian to simultaneously speed up the gradient search and provide higher confidence in the results.

As an example of EMI data with overlapping responses, Fig. 26 in Appendix A.2 shows typical frequency domain data from a GEM-3 acquired over multiple buried targets [14]. Figure 30 (top left subfigure) also show GEM-3 data from a 105mm UXO obfuscated by a layer of discrete clutter affixed to plywood. Even though we do not plan to use the GEM-3 for this research, evident in this data is the need for robust processing which identifies and classifies discrete anomalies and higher quality data addressing both positional and instrument noise.

The challenges involved with the discrimination of anomalies in close proximity are significant and persistent. In all prior cases, data quality in terms of the

signal to noise ratio (SNR), positional inaccuracies, and data completeness (e.g. survey spacing), has been a significant factor which limits the success of the various models.

4 Technical Approach

4.1 Canonical Targets

This project shares one early goal with two other projects (MR-1662 under SAIC, and MR-1669 under BAE) which started in the same FY as this MR-1664: to fabricate a set of canonical targets as a basis and baseline for measurements and testing. These targets have been fabricated and consist of two sets of spheroids and spheres combined together under the stewardship of Dan Steinhurst at NOVA Research: an old set made by Dr. Ben Barrowes while at MIT in 2003 and consists of smaller spheroidal and spherical targets under 25cm in the longest dimension (see Table 1 and Fig. 1), and a new set fabricated in 2009 and 2010 for these projects subcontracted through Delpsi, LLC (see Table 2). Figures 2–3 shows the spheroids from the second, larger set. Details on these targets are in Sec. 4.1. Data collected from the TEMTADS instrument over these canonical targets is summarized in Sec. 5.1 while data collected over multitarget UXO configurations with the MPV2 instrument in included in Sec. 5.3.

	comp.	type	axis ($2a$)	axis ($2b$)	nominal $e = b/a$
S1	Iron	sphere	90.62mm	90.62mm	1
S2	Steel	PS	30.02mm	182.19mm	6
S3	Steel	PS	29.94mm	90.28mm	3
S4	Steel	PS	14.97mm	90.76mm	6
S5	Steel	OS	29.32mm	4.56mm	1/6
S6	Steel	OS	29.59mm	9.65mm	1/3
S7	Steel	sphere	29.87mm	29.87mm	1
S8	Steel	OS	89.85mm	28.39mm	1/3
S9	Steel	OS	89.95mm	15.32mm	1/6
A1	Al	PS	30.17mm	180.23mm	6
A2	Al	PS	29.9mm	91.29mm	3
A3	Al	PS	15.04mm	91.14mm	6
A4	Al	OS	29.36mm	4.34mm	1/6
A5	Al	OS	29.36mm	8.88mm	1/3
A6	Al	sphere	29.91mm	29.91mm	1
A7	Al	OS	89.92mm	30.38mm	1/3
A8	Al	OS	89.98mm	15.94mm	1/6

Table 1: Physical dimensions of steel and aluminum spheroids. PS $\Rightarrow$ Prolate Spheroid. OS $\Rightarrow$ Oblate Spheroid.

Figure 1: Spheroid collection used for testing. Specifications are listed in Table 1.

	comp.	type	nominal axis ($2a$, cm)	nominal axis ($2b$, cm)	nominal $e = b/a$
SS1	steel	sphere	10	10	1
SS2	steel	sphere	15	15	1
SP1	steel	sphere	10	20	2
SP2	steel	prolate	6.67	20	3
SP3	steel	prolate	5	20	4
SP4	steel	prolate	4	20	5
SP5	steel	prolate	6	30	5
SP6	steel	prolate	12.5	50	4
SP7	steel	prolate	10	50	5
SP8	steel	prolate	10	30	3
SP9	steel	prolate	15	30	2
SP10	steel	prolate	7.5	30	4
SO1	steel	oblate	20	8	2/5
SO2	steel	oblate	20	4	1/5
SO3	steel	oblate	20	2.67	1/7.5
SO4	steel	oblate	20	2	1/10
AS1	aluminum	sphere	10	10	1
AS2	aluminum	sphere	15	15	1
AP1	aluminum	sphere	10	20	2
AP2	aluminum	prolate	6.67	20	3
AP3	aluminum	prolate	5	20	4
AP4	aluminum	prolate	4	20	5
AP5	aluminum	prolate	6	30	5
AP6	aluminum	prolate	12.5	50	4
AP7	aluminum	prolate	10	50	5
AP8	aluminum	prolate	10	30	3
AP9	aluminum	prolate	15	30	2
AP10	aluminum	prolate	7.5	30	4
AO1	aluminum	oblate	20	8	2/5
AO2	aluminum	oblate	20	4	1/5
AO3	aluminum	oblate	20	2.67	1/7.5
AO4	aluminum	oblate	20	2	1/10

Table 2: Physical dimensions of larger set of steel and aluminum spheroids fabricated in 2009-2010. First letter of designation is material (A=Aluminum, S=steel), second letter is shape (S=Sphere, P=Prolate, O=Oblate), and a number designation.

(a) SS1 and AS1

(b) SS2 and AS

(c) SP1 and AP1

(d) SP2 and AP2

(e) SP3

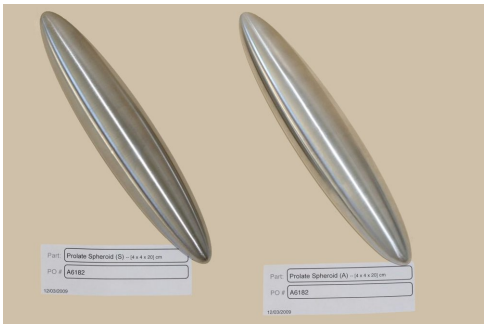

(f) SP4 and AP4

(g) SP5 and AP5

(h) SP6

Figure 2: Larger steel spheroids SS1-SP6. Specifications are listed in Table 2.

(a) SP7

(b) SP8

(c) SP9

(d) SP10

(e) SO1 and AO1

(f) SO2 and AO2

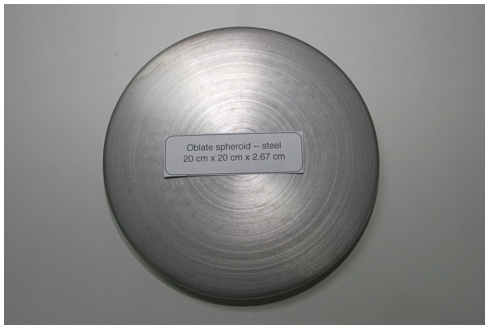

(g) SO3

(h) SO4

Figure 3: Larger steel spheroids SP7-SO4. Specifications are listed in Table 2.

4.2 Multiple Dipole Inversion Using Jacobian Gradient Search

The simultaneous detection and identification of multiple targets using electromagnetic induction time-domain sensors remains a challenge due to the fast decay of the magnetic field with sensor-target distance. For example, the signal from a weak yet shallow target or clutter item can overshadow that from a much larger yet deeper UXO, potentially resulting in erroneous localization and/or identification. We propose in this paper a method based on the Gauss-Newton algorithm for the inversion of multiple targets within the field of view of sensors operating at electromagnetic induction – EMI – frequencies (tens of Hertz to a few hundred kHz). In order to minimize the number of unknowns to invert for, the polarizability tensor is written as a time-independent orientation matrix multiplied by a time-dependent diagonal intrinsic polarizability tensor. Similarly, position is supposed to be time independent so that both position and orientation angles are inverted only once using all time channels collected by the instrument. Moreover, using the dipole approximation, we are able to compute the Jacobian in closed form for instruments with either square or circular primary field coils, thus contributing to the speed of the algorithm. Validating results are shown based on measurement data collected with two EMI sensors on various types of UXO.

4.2.a Introduction

Numerous military campaigns and warfare practice over the last decades have left millions of acres of land contaminated worldwide with unexploded ordnance (UXO), projectiles with explosive cores and metallic shells that did not explode upon impact and penetrated into the ground. The cleaning of these fields is currently a daunting and hugely expensive task that consumes a budget of several million dollars in the United States alone. Such prohibitively large cost is due to a very large false-alarm rate associated with the detection of UXO with current remote sensing technologies. Differentiating between unexploded and exploded ordnance is a technological challenge that is yet to be overcome in realistic field situations, where clutter and/or geological factors can significantly jam the signals used by remote sensing algorithms. As a result, current cleaning campaigns are based on overly simple metal detection schemes with little discrimination involved, yielding hugely time consuming and expensive campaigns which result most of the time in the excavation of harmless objects.

In parallel, researchers have spent decades investigating technologies and re-

fining algorithms to detect and discriminate metallic subsurface objects better. For example radar sensors operating in the microwave regime, which have been so successful when pointing to the sky, have been turned upside down to send and receive signals into and from the ground. Advanced signal processing techniques have proven the usefulness of this approach [15, 16], but also revealed its limitations due to the variations in soil surfaces and volume compositions which quickly obscure the signatures of the subsurface targets. As an alternative, electromagnetic induction (EMI) which utilizes magnetic fields at much lower frequencies (from tens of Hertz to a few hundred kHz) has proven remarkably robust. The associated magneto-quasistatic regime ensures that displacement currents are negligible compared to conduction currents in the metallic targets. The soil, assumed here to be non-magnetic and non-conductive, is transparent so that the UXO can be simply considered in free space. Various models have been proposed, from the simple but effective dipole model [17–20], to more elaborated theoretical studies on canonical shapes [21–23] as well as more flexible numerical models [24, 25]. The purpose of these various techniques is to improve the discrimination capabilities of UXO in realistic environments [26–29].

A major drawback of the EMI regime, however, is its sharp field decay (approximately as $1/r^3$ at large distances compared to the primary coil size, with r being the target-sensor distance) which makes it difficult to use EMI frequencies at ranges beyond a few times the size of the coils or when identifying multiple UXO in close proximity to one another as well as in close proximity to large clutter items. For example, even a small but shallow metal object can overshadow the signal of a deeper UXO producing an erroneous classification. A related problem occurs when targets of similar sizes are buried alongside one another at comparable depths [7]. In both situations, the detection and identification can be considerably improved by considering a multi-target configuration, whereby multiple time signatures are simultaneously inverted for and used in the decision scheme. One of the first attempts along this direction collaboratively used EMI and radar signals [9, 10]. This approach, however, revealed to be both time consuming and costly due to the combination of two sets of hardware and two analysis algorithms involved. Other attempts concentrated on using only EMI data with signal processing techniques for sources separation [5]. Successful results were reported on synthetic data (i.e. computer generated) while more validation is expected using real UXO and EMI sensors. Similarly, an independent component analysis revealed the possibility of extracting the signature of a UXO in the presence of

multiple clutter items, but the method concentrated on the specific situation of known UXO, i.e. a known signature which had to be extracted from a sum of multiple signatures [30]. More recently, positions, orientations, and time dependent polarizabilities were inverted on two-target configurations from both synthetic as well as sensor data [31]. The method, based on a multi-start search and separation of the linear and nonlinear parameters, was shown to yield good agreement with ground truth. However, as the authors point out, the strong nonlinearity of the problem required a good initial guess, which was provided by sampling a region of interest. This requirement could be alleviated by using a multiple signal classification approach [32, 33] for position estimation (nonlinear part) followed by a direct solution of the polarizabilities (linear part) using either a least square method [34], a Kalman filter approach [35], or other. Yet, this approach presents some limitation when monostatic data are used in the inversion process.

Trying to alleviate some of these pitfalls, we propose in this paper an algorithm significantly improved compared to our previous work [36]: factorization of the orientation angles from the time dependent unknown vector, incremental step size in the Gauss-Newton algorithm, analytical computation of the Jacobian matrix for square and circular primary field coils, and solution selection. The resulting new algorithm shows robustness to initial conditions that removes the need of user defined regions of interest, numerical stability that reduces the number of realizations necessary to filter out local minima solutions, and computational speed. The method is here extensively validated using measured data from two types of EMI sensors (MPV and TEMTADS) on a variety of UXO.

4.2.b Problem configuration and EMI sensors

We consider the problem illustrated in Figure 4, whereby a sensor at position $\bar{r}_s$ illuminates multiple targets described by their positions $\bar{r}_\ell = \hat{x}x_\ell + \hat{y}y_\ell + \hat{z}z_\ell$, elevations θ_ℓ and azimuths ϕ_ℓ where $\ell = 1,\ldots,N$ ($N = 3$ is shown in the figure). We suppose all N targets to be bodies of revolution, modeled as a three-axis dipole with parameters $\bar{r}_\ell$, θ_ℓ, ϕ_ℓ and intrinsic polarizabilities $\overline{\overline{\beta}}_\ell$ (see subsequent Eq. (4.5c)). The transmitter and receiver sensors are incorporated into our algorithm to closely model the hardware configuration of either the TEMTADS [37, 38] or the MPV [39] instruments. receiver sensors separated by 40 cm (center to center) in the (xy) plane and collecting z components of the secondary magnetic field induced by the target. Each sensor is composed of a square trans-

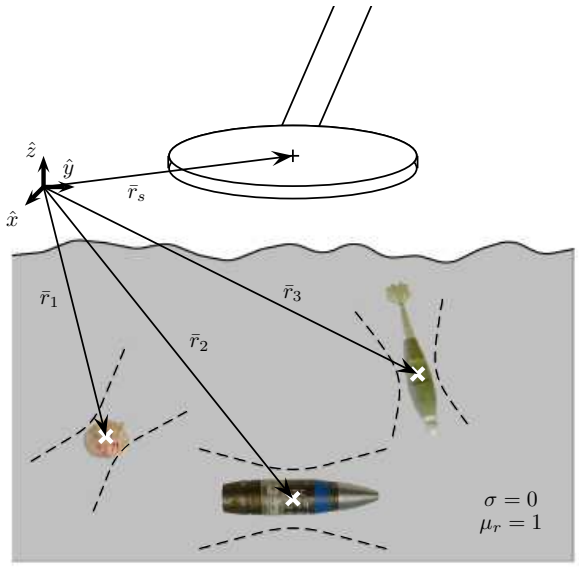

Figure 4: Problem configuration: an EMI sensor surveys an area where N targets are buried ($N = 3$ in the figure). The unknowns of the problem are the targets (intrinsic) polarizabilities themselves as well as their positions $\bar{r}_\ell$ and orientations (θ_ℓ, ϕ_ℓ). The soil is supposed to be non-conductive ($\sigma = 0$) and non-permeable ($\mu_r = 1$).

mitting coil (side dimension: 35 cm) and a co-centered square receiving coil (side dimension: 25 cm) which are time decoupled: during the first half of the cycle, the transmitting coils emits a primary field which excites all metals in its vicinity whereas during the second half of the cycle, the receiving coil measures the derivative of the flux generated by all ringing metals. The hardware electronics integrates the flux to yield a quantity proportional to the magnetic field which is measured typically after the first 100 μs to let the instrument transients die away. The targets themselves typically ring for many milliseconds so that measurements are gathered until about 25 ms logarithmically sampled in 120 time channels. Measurements can be performed in either a monostatic mode, in which case all the 25 sensors sequentially transmit and receive yielding 25 data points, or in a bistatic mode in which case each transmitter fires sequentially and measurements are gathered by all 25 receivers yielding 625 data points. We model the transmitters as square current loops whose primary field can be written as the addition of four sections of straight wire which all carry a unit constant current. The primary field from each wire is given by

$$\bar{H}^{\text{wire}} = \frac{\hat{s}}{4\pi|\bar{s}|}(\hat{r}_1 - \hat{r}_2) \cdot \hat{r}_{12} \tag{4.1}$$

where a hat denotes a unit vector and a bar denotes a regular vector, $\hat{r}_1$ and $\hat{r}_2$ are the unitary vectors between each extremities of the straight wires and the observation point, $\bar{r}_{12} = \bar{r}_2 - \bar{r}_1$, and $\bar{s} = \hat{r}_{12} \times \bar{r}_1$. The received signal at each receiver is simply computed by integrating the secondary magnetic field over the surface of the corresponding receiving square coil.

The MPV (Man Portable Vector) [39] sensor is very different from the TEMTADS in that it is much smaller and lighter. It uses a pair of coaxial circular transmitting coils (of radius 37.5 cm and vertical separation 15.6 cm) and a series of five square receiving coils (of side dimensions 10 cm) which can measure all components of the secondary field. The primary field is modeled as that produced by a circular current loop of radius a and unit current. In the cylindrical coordinate system, the field at (ρ, z) is written as [18, 40]:

$$H_\rho(\rho,z) = \frac{1}{2\pi} \frac{1}{\sqrt{(a+\rho)^2+z^2}} \frac{z}{\rho} \left[\frac{a^2+\rho^2+z^2}{(\rho-a)^2+z^2} E(k) - K(k) \right], \tag{4.2a}$$

$$H_z(\rho,z) = \frac{1}{2\pi} \frac{1}{\sqrt{(a+\rho)^2+z^2}} \left[\frac{a^2-\rho^2-z^2}{(\rho-a)^2+z^2} E(k) + K(k) \right], \tag{4.2b}$$

where $K(k)$ and $E(k)$ are the elliptic integrals of the first and second kind, respectively, with $k^2 = 4a\rho / \left[(\rho+a)^2+z^2\right]$. The received signal is computed by integrating the secondary magnetic field over the surface of the receiving perpendicular square coils. Like for the TEMTADS, measurements are gathered during off-time cycles (when the primary field is turned off), between about 0.4 ms and 23 ms sampled in 30 time channels. Inherent to its construction, the operating mode of the MPV is a mixture of monostatic and bistatic mode, typically coined multi-static (the receivers are tied to the transmitter but not collocated). Advantages compared to the TEMTADS are its vectorial property and its maneuverability in complex terrain whereas its disadvantages are its smaller field of view and the necessity of tracking its position and orientation during data acquisition.

4.2.c Data analysis

The fast field decay in the EMI regime ensures that near field effects are confined to a very small volume surrounding the buried target. As a consequence, the secondary field at the sensor location is almost identical to that of a triaxial dipole,

for which the magnetic field $\bar{H}$ is given by [18]:

$$\bar{H}(\bar{r}_s) = \frac{1}{4\pi r_{ts}^3}\left[\frac{3\bar{r}_{ts}(\bar{r}_{ts}\cdot\bar{m})}{r_{ts}^2} - \bar{m}\right] \tag{4.3}$$

where $\bar{m} = \hat{x}m_x + \hat{y}m_y + \hat{z}m_z$ is the dipole moment of the target, $\bar{r}_t$ is the target location, $\bar{r}_s$ is the sensor location, $\bar{r}_{ts} = \bar{r}_s - \bar{r}_t$ and $r_{ts} = ||\bar{r}_{ts}||$. It should be mentioned that the dipole analysis remains an approximation which has proven accurate in the overwhelming majority of UXO configurations. However, its limitation is particularly obvious with heterogeneous targets or when multiple targets are in very close proximity to one another, typically within a sub-centimeter distance, with one or both targets being ferrous [41]. In this situation, coupling between eddy currents of the two objects can happen at a level sufficient to alter the secondary magnetic field at the receiver location [42]. Such configuration is, however, more theoretical than practical and to our knowledge, has not been encountered beyond laboratory tests. As a consequence, we suppose here that the separation between the targets is sufficient to ensure that the various UXO respond as independent dipoles with no coupling effects [43]. Within such independent scattering approximation, the magnetic field of N targets located at $\bar{r}_\ell$ ($\ell = 1,\ldots,N$) and with dipole moments $\bar{m}_\ell$ is simply obtained as the algebraic sum of Eq. (4.3):

$$\bar{H}(\bar{r}_s) = \sum_{\ell=1}^{N} \frac{1}{4\pi r_{\ell s}^3}\left[\frac{3\bar{r}_{\ell s}(\bar{r}_{\ell s}\cdot\bar{m}_\ell)}{r_{\ell s}^2} - \bar{m}_\ell\right]. \tag{4.4}$$

Note that we assume N to be known in Eq. (4.4), which is an assumption further discussed in Section 4.2.e. The dipole moment $\bar{m}_\ell$ is obtained from the self-polarizability $\overline{\overline{\beta}}_\ell$ of the target along three directions, weighted by the primary field at the target location. If, in addition, the target is rotated with respect to the global reference frame, the rotation angles need to be incorporated. Restricting ourselves to bodies of revolution as most UXO are, the dipole moment $\bar{m}_\ell$ can be written as

$$\bar{m}_\ell = \overline{\overline{\Lambda}}_\ell^{T} \cdot \overline{\overline{\beta}}_\ell \cdot \overline{\overline{\Lambda}}_\ell \cdot \bar{H}^{pr}(\bar{r}_\ell) \tag{4.5a}$$

where

$$\overline{\overline{\Lambda}}_\ell = \begin{pmatrix} \cos\theta_\ell\cos\phi_\ell & \cos\theta_\ell\sin\phi_\ell & -\sin\theta_\ell \\ -\sin\phi_\ell & \cos\phi_\ell & 0 \\ \sin\theta_\ell\cos\phi_\ell & \sin\theta_\ell\sin\phi_\ell & \cos\theta_\ell \end{pmatrix} \tag{4.5b}$$

is the rotation matrix with the angles θ_ℓ and ϕ_ℓ,

$$\overline{\overline{\beta}}_\ell = \begin{pmatrix} \beta_{x_\ell} & 0 & 0 \\ 0 & \beta_{y_\ell} & 0 \\ 0 & 0 & \beta_{z_\ell} \end{pmatrix}, \tag{4.5c}$$

where $(\beta_{x_\ell}, \beta_{y_\ell}, \beta_{z_\ell})$ are the time-dependent polarizabilities along the three directions of the reference frame local to the target, and $\bar{H}^{pr}(\bar{r}_\ell)$ is the primary field at the target location. Note that two components of $\overline{\overline{\beta}}_\ell$ are expected to be identical due to the BOR assumption, even though this property is not enforced in Eq. (4.5c). For example, in a bistatic configuration, the transmitter remains at a unique location while the receiver spans a series of measurement points. As a consequence, the primary field $\bar{H}^{pr}(\bar{r}_\ell)$ is unique and so is $\bar{m}_\ell$. In a monostatic configuration, however, where the transmitter and receivers are collocated and span together the measurement points, $\bar{H}^{pr}(\bar{r}_\ell)$ varies from point to point, and so does $\bar{m}_\ell$. The polarizability tensor $\overline{\overline{\beta}}_\ell$, however, is invariant and can be used by a classifier for each target.

Our inversion algorithm is based on a Gauss-Newton solution of the normal equation assuming N targets present in the field of view of the sensor. The simultaneous inversion of the time-independent position, orientation, and time-dependent polarizabilities of the targets is expressed as a least-squares minimization between the measured field and the predicted field computed from Eq. (4.4). Hence, the unknown vector is written as

$$\mathbf{x} = [\mathbf{a}_1 \ldots \mathbf{a}_\ell \ldots \mathbf{a}_N \, \mathbf{b}_1 \ldots \mathbf{b}_\ell \ldots \mathbf{b}_N]^T, \tag{4.6a}$$

$$\mathbf{a}_\ell = [x_\ell \; y_\ell \; z_\ell \; \theta_\ell \; \phi_\ell]^T, \tag{4.6b}$$

$$\mathbf{b}_\ell = [\beta_{x_\ell}^{t_1} \; \beta_{y_\ell}^{t_1} \; \beta_{z_\ell}^{t_1} \; \ldots \beta_{x_\ell}^{t_{N_{tc}}} \beta_{y_\ell}^{t_{N_{tc}}} \beta_{z_\ell}^{t_{N_{tc}}}]^T, \tag{4.6c}$$

where t_j $(j = 1, \ldots, N_{tc})$ denotes the time channels and where the subscript 'T' denotes the transpose. Eq. (4.6c) indicates that the algorithm solves for a single position and a single orientation per target, with multiple polarizabilities across the time history of the transmitter for all targets simultaneously. Note that it is also possible to invert for a more general polarizability tensor with six independent elements [31, 44, 45]. Although such approach has been shown to be valid and accurate, it is not adopted here: inverting a full tensor at each time channel is analogous to inverting for the rotation angles at each time channel. Within a good approximation, however, these angles can be considered time independent so that

we factor them out of the polarizability tensor and included them in the time independent part of the minimization vector, thus drastically reducing the number of unknowns to invert for. Note that similarly, the algorithm inverts for a unique position rather than a time-dependent position at every time channel. Considering the position and angles to be time independent is an approximation justified in practice. Indeed, although various parts of the UXO may respond differently in time, effectively yielding slightly different positions and orientations of the triaxial dipole used to best match the measured secondary field, we have found this effect to be small in the cases considered in this paper: inverting the positions at every time channels yields similar estimates except at later times when the field values reach the noise level (data not shown).

The task of the minimization algorithm is to estimate the unknown parameter $\mathbf{x}$ so as to minimize the sum of squares

$$\min_{\mathbf{x}} S = \min_{\mathbf{x}} \left(\Delta \bar{H}_z^T \, \Delta \bar{H}_z \right) \tag{4.7}$$

where $\Delta \bar{H}_z = (\bar{H}_z^{\text{mea}} - \bar{H}_z)$ with $\bar{H}_z^{\text{mea}}$ and $\bar{H}_z$ being the measured and computed z components of the magnetic field, respectively. If needed, the addition of other components of the magnetic field to the minimization problem is straightforward (e.g. the TEMTADS measures only H_z whereas the MPV measures all three components). The corresponding normal equation is written as

$$\bar{\bar{J}}_z^{\,T} \bar{\bar{J}}_z \cdot \Delta \mathbf{x} = \bar{\bar{J}}_z^{\,T} \cdot \Delta \bar{H}_z \tag{4.8}$$

where $\Delta \mathbf{x} = \mathbf{x}^{i+1} - \mathbf{x}^i$ is the unknown vector which provides the updated quantities of $\mathbf{x}$ at each iteration, i is the iteration number, $\bar{\bar{J}}_z$ is the Jacobian matrix. The Gauss-Newton update equation is therefore

$$\mathbf{x}^{i+1} = \mathbf{x}^i + \Delta \mathbf{x} = \mathbf{x}^i + \left(\bar{\bar{J}}_z^{\,T} \bar{\bar{J}}_z \right)^{-1} \bar{\bar{J}}_z^{\,T} \cdot \left(\bar{H}_z^{\text{mea}} - \bar{H}_z \right) \tag{4.9}$$

The vector notation used on $\bar{H}_z^{\text{mea}}$ and $\bar{H}_z$ refers to the fact that the magnetic field is measured and computed over a series of K observation points. The Jacobian matrix is therefore a block matrix of size $[N_{tc} \times K, N(5+3N_{tc})]$ where N_{tc} is the number of time channels. Splitting the Jacobian matrix into time independent and time dependent parts, we write:

$$\bar{\bar{J}}_z = \left[\bar{\bar{A}}_z \, , \, \bar{\bar{B}}_z \right] \tag{4.10}$$

where $\overline{\overline{A}}_z$, of size $[N_{tc} \times K, 5N]$, gathers the derivatives of the computed $\bar{H}_z$ field with respect to the three positions and two angles across all observation points and time channels. Assuming $N = 1$ for the sake of simplicity of notation in this example:

$$\overline{\overline{A}}_z = \begin{pmatrix} \overline{\overline{A}}_z^{t_1} \\ \vdots \\ \overline{\overline{A}}_z^{t_j} \\ \vdots \\ \overline{\overline{A}}_z^{t_{N_{tc}}} \end{pmatrix} \text{ with } \overline{\overline{A}}_z^{t_j} = \begin{pmatrix} \bar{A}_{z_1}^{t_j} \\ \vdots \\ \bar{A}_{z_\ell}^{t_j} \\ \vdots \\ \bar{A}_{z_K}^{t_j} \end{pmatrix} \tag{4.11a}$$

and

$$\bar{A}_{z_\ell}^{t_j} = \left[\frac{\partial}{\partial x_\ell} \; \frac{\partial}{\partial y_\ell} \; \frac{\partial}{\partial z_\ell} \; \frac{\partial}{\partial \theta_\ell} \; \frac{\partial}{\partial \phi_\ell} \right] H_z^{t_j}(\bar{r}_\ell) \tag{4.11b}$$

where $H_z^{t_j}(\bar{r}_\ell)$ is the z component of the magnetic field obtained from Eqs. (4.4) and (4.5) at time channel t_j. The matrix $\overline{\overline{B}}_z$ is a block diagonal matrix where each block has a size $[N_{tc} \times K, 3N_{tc}]$ (still under the assumption of $N = 1$) and gathers the derivatives of the computed $\bar{H}_z$ field with respect to the three polarizabilities:

$$\overline{\overline{B}}_z = \text{diag}[\overline{\overline{B}}_z^{t_1}, \ldots, \overline{\overline{B}}_z^{t_j}, \ldots, \overline{\overline{B}}_z^{t_{N_{tc}}}] \text{ with } \overline{\overline{B}}_z^{t_j} = \begin{pmatrix} \bar{B}_{z_1}^{t_j} \\ \vdots \\ \bar{B}_{z_\ell}^{t_j} \\ \vdots \\ \bar{B}_{z_K}^{t_j} \end{pmatrix} \tag{4.12a}$$

and

$$\bar{B}_{z_\ell}^{t_j} = \left[\frac{\partial}{\partial \beta_{x_\ell}} \; \frac{\partial}{\partial \beta_{y_\ell}} \; \frac{\partial}{\partial \beta_{z_\ell}} \right] H_z^{t_j}(\bar{r}_\ell) \tag{4.12b}$$

The formulation outlined above is straightforward to generalize to the case of $N > 1$ as well as when all components of the magnetic field are known (for example if the MPV sensor is used) by simply stacking the Jacobian matrices and right-hand side vectors corresponding to other components, and generalizing the unknown vector $\mathbf{x}$. Note that all the derivatives are straightforward to compute except those with respect to position since they require the derivative of the primary field as well, in view of Eq. (4.5a). This task can still be performed analytically for both the TEMTADS and MPV sensors using Eqs. (4.1) and (4.2) and a pre-

cise knowledge of the sensors' geometries, which contributes to the computational efficiency of the algorithm.

The actual implementation of Eq. (4.9) is slightly modified by the addition of a weighting factor $\alpha \leq 1$ in order to control the step size:

$$\mathbf{x}^{i+1} = \mathbf{x}^{i} + \alpha\left(\bar{\bar{J}}_z^{\,T}\bar{\bar{J}}_z\right)^{-1}\bar{\bar{J}}_z^{\,T}\cdot\left(\bar{H}_z^{\text{mea}} - \bar{H}_z\right) \tag{4.13}$$

Empirical investigations revealed an increasing importance of α as the number of targets to invert for increased: from practically unnecessary for $N = 1$ to important for $N \geq 3$. While further analytical investigations might be necessary to determine the optimal α for each configurations, results reported hereafter have been obtained with $\alpha = 0.5$, which appears to offer a good compromise between accuracy and convergence speed.

4.2.d Inversion results

Despite an extensive validation campaign on synthetic data, we concentrate and only present here results from data that have been acquired by real sensors on real UXO. Data have been collected using both the TEMTADS [46] and MPV instruments [47] and the inversion results are presented in the following two sections on various multi-target configurations. It is important to keep in mind that measurements are performed on real UXO which therefore have certain physical dimensions, whereas the algorithm is inverting for one tri-axial dipole per UXO. The location of these equivalent dipoles is not precisely defined: it is close to the center of the target if the latter is buried horizontally (i.e. parallel to the sensor), whereas it migrates toward the tip for vertical targets where one extremity is closer to the sensor than the other. The positions also depend on the composition, geometry, and external features of each target such as fins, conductive rings, etc. The exact location at which a single tri-axial dipole should be located in order to best reproduce the secondary field of a given UXO is therefore not expected to match exactly the positions recorded at the data acquisition stage (which correspond typically to the exact center or exact tip of the UXO). The accuracy of the subsequent results should be judged with these considerations in mind.

4.2.d.(1) MPV data The MPV is a vectorial multi-static EMI instrument which collects data as it is waved above the surface. Due to its intrinsic portable nature, the trajectory of the MPV as well as its orientation (e.g. pitch, roll, and yaw) need

to be tracked during the entire data acquisition time. The data set thus collected is then converted into components of the magnetic field along three pre-defined directions, and subsequently processed by our algorithm. The results reported hereafter have been obtained using the vectorial information of all five sensors, even though more in depth studies showed that not all carry a critical information necessary for proper inversion (data not shown).

A first series of validating tests of our MPV model was performed on single targets and yielded good results in all the cases considered for both the positions, orientations, and time dependent polarizabilities. Table 3 lists a few cases with the corresponding inverted positions and orientations which show a reasonable agreement with the ground truth. We recall here that the ground truth values typically correspond to distances to the center of the UXO, which might be a few centimeters deeper from the optimized location of an equivalent dipole (nearer to the sensor). For example, the elevation of the 60-mm UXO was set to $\theta = 270$ degrees, which corresponds to the target being horizontal. The exact location of the principal responding magnetic dipole of the target may not correspond to the geometrical center of the actual target. Therefore, a first order correction to the inverted depth for this case to account for the radius of the target, i.e. 30 mm, augments the inverted depth from 48 cm to 51 cm, in good agreement with the ground truth. Corrections to other targets are not as straightforward to incorporate because of the non-trivial elevation angles. The largest deviation in depth amounts to 10 cm and occurs with the 105-mm with $\theta = -19$ degrees. The small elevation indicates that the target is close to vertical so that an important deviation between the center position and the location of the equivalent dipole is expected, especially because this target is very long. In addition to the mismatch between the center of the target and the location of its equivalent dipole, part of the discrepancies in Table 3 can also be attributed to measurement and instrument noise while yet another part could be due to algorithmic inaccuracies (for example due to a too small data set to optimize the unknown vector to a desired level of accuracy). The overall good results, however, suggest that the algorithm is effective at inverting MPV data. This conclusion is also supported by the time dependent polarizabilities obtained for these cases, a subset of which is shown in Figure 5. As expected, the 81-mm UXO shows one polarizability element consistently stronger than the other two which are almost identical and reveal a geometric azimuthal symmetry. The BLU26 exhibits similar characteristics but the three polarizabilities are closer to each other due to the close to spherical shape of this UXO (see inset).

Target	Length	Ground truth					Inverted results				
		[cm]			[degrees]		[cm]			[degrees]	
	[mm]	x	y	z	θ	ϕ	x	y	z	θ	ϕ
Al sphere		0	22	26	-	-	0	22	29	-	-
Brass sphere		0	22	26	-	-	0	22	28	-	-
Steel sphere		0	22	26	-	-	0	22	28	-	-
81-mm	490	-23	22	52	-18	0	-14	22	50	-20	-10
105-mm	642	-20	22	63	-19	180	-12	23	50	-30	176
BLU26	70.31	0	22	38	0	0	0	22	34	-	-
57-mm	170.47	5	22	55	307	180	4	22	51	310	160
60-mm	245	0	22	51	270	0	0	22	48	260	7

Table 3: Inverted positions of single targets using data from the MPV instrument. The time signatures for the 81-mm and the BLU26 are shown in Figure 5. Positions are rounded to the closest integer.

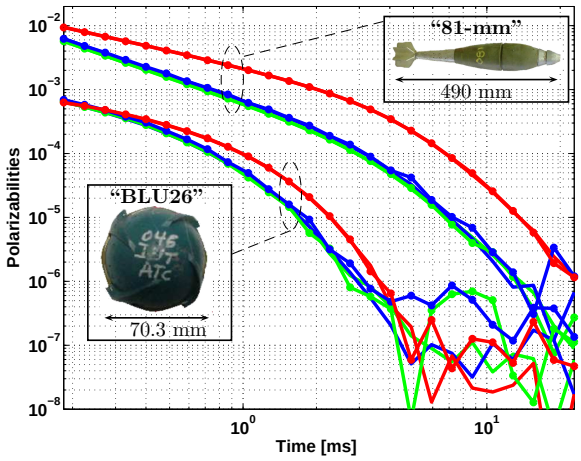

Figure 5: Time domain polarizabilities for two types of UXO (81-mm and BLU26) measured and inverted separately from MPV data.

Two-target results present mitigated yet consistent results within the data set available to us.Two configurations were analyzed: that of two 40-mm UXO at the same depth, and that of a 40-mm along with 81-mm UXO at varying depths, both cases for different lateral separations. Inverted positions, summarized in Table 4, indicated a good performance when the targets are at the same depth, with yet improved accuracy for larger lateral separations as intuitively expected. This is evident from the inverted polarizabilities of the two 40-mm targets, shown in Figure 6(a): while the four strong components (two targets in two configurations) are almost identical in both cases, one of the weak components is slightly under-estimated for dx=25 cm (circle marks). The good performance at identical depth is somewhat maintained with the two different targets, despite a small error in the inverted lateral separation which can be mostly attributed to the physical width of the targets. Incorporating this correction of about 6 cm, the inverted separation would be about 21 cm instead of the measured 25 cm. The overall results worsen, however, when the two targets are at different depths, with z_2 in Table 4 often under-estimated. The polarizabilities, shown in Figure 6(b) reflect this behavior: while the larger target is consistently well predicted, the weaker one is better predicted at similar depth (see the dipping weak component for dz=25 cm, indicating a sign change and thus a weak corresponding component of the secondary magnetic field).

In depth investigations of these cases suggested that the data set itself might not be totally consistent from grid point to grid point, but contains variations that are likely at the origin of some of the errors in the inversion results. As a matter of fact, although the natural operating mode of the MPV is to be waved above the targets, data provided to us has been collected in an inverted configuration, whereby the MPV was held fixed and the targets were moved on a 5×5 square grid with 20 cm separation between adjacent points. Repeatability between grid point therefore cannot be guaranteed since the two targets can easily move with respect to each other, either in distance or in orientation. Since our algorithm assumes an invariant configuration from grid point to grid point (akin to when the targets are buried), these errors would induce inversion inaccuracies. Yet, the overall good agreement between the inverted results and reported ground truth confirm the possibility of using the MPV for the detection and classification of multi-targets.

4.2.d.(2) TEMTADS data measurement campaign using the TEMTADS sensor has been undertaken by the Naval Research Laboratory on one, two, as well as

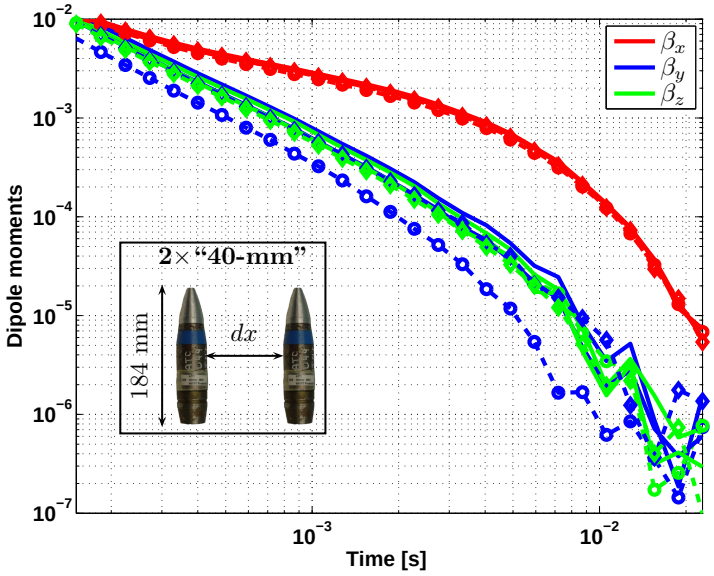

(a) Two 40-mm UXO inverted in two configurations: (dx,dz)=(25,0) and (40,0) cm. The visibly weaker components (circle marks) corresponds to dx=25 cm.

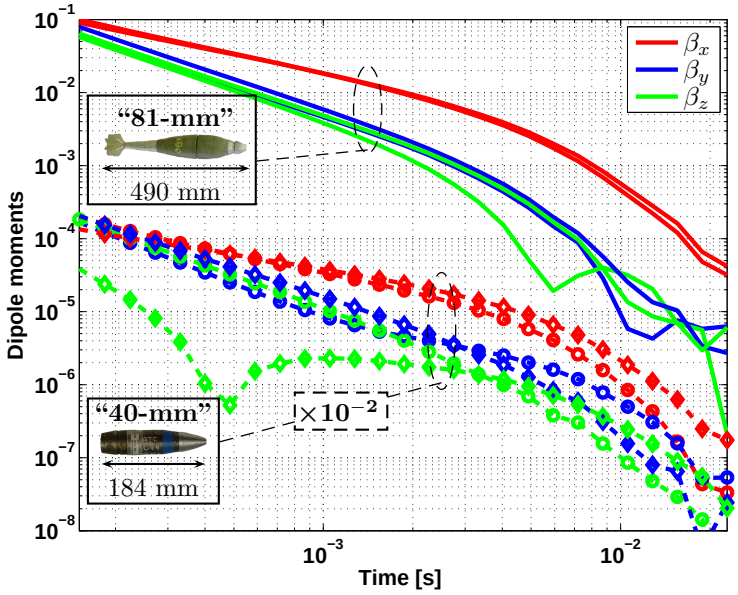

(b) 81-mm and 40-mm UXO inverted in two configurations: (dx,dz)=(25,0) and (25,25) cm. The weaker and dipping component (diamond marks) corresponds to dz=25 cm.

Figure 6: Time domain polarizabilities for two two-target configurations measured by the MPV. Inverted positions are summarized in Table 4.

UXO	Truth [cm]						Inverted [cm]					
	x_1	y_1	z_1	x_2	y_2	z_2	x_1	y_1	z_1	x_2	y_2	z_2
40-mm & 40-mm	0	0	40	25	0	40	2	−1	40	23	0	38
40-mm & 40-mm	0	0	40	40	0	40	1	−1	39	40	−2	39
81-mm & 40-mm	0	0	40	25	0	40	0	0	42	18	0	40
81-mm & 40-mm	0	0	65	25	0	40	0	0	43	22	0	38

Table 4: Inversion results on two-target configurations from data collected by the MPV sensor. Positions are rounded to the closest integer.

three-target configurations. The targets of interest were a 4.2-inch mortar, a nose cone, and a baseplate whose time dependent polarizabilities are represented in Figure 7 when they are inverted as separate targets. Like the 81-mm previously, the mortar exhibits a typical signature of a UXO, whereby one polarizability dominates the other two which are almost identical, indicating that the target is a body of revolution with a preferential direction. The nose cone produces a signal that is about two orders of magnitude inferior to the mortar, with a mostly log-log linear time decay indicating a strong ferrous component. In addition, the three polarizabilities are comparable which suggests a somewhat homogeneous shape in three directions, akin to a sphere. The baseplate produces a signal of comparable magnitude to the mortar with the strongest dipole switching in time from the $\hat{x}$ direction to the $\hat{z}$ direction. These signatures have been obtained using the method presented in the previous section and have been independently validated [48, 49]. The inverted positions, listed in the captions of Figure 7, match the true values with a centimeter accuracy and validate our algorithm as well as the associated TEMTADS model in the case of single targets. We emphasize also the fact that the inverted angles are typically within a few degrees of their expected values.

Two-target configurations consisted of combining the mortar with one of the other two targets and varying their respective lateral distances while keeping their depths constant. The lateral distances were varied from $x = 0$ cm to $x = 100$ cm at 10 cm intervals (yielding 11 configurations). At $x = 0$ the targets are immediately on top of each other, which is known to be a challenging configuration to invert due to the strong EMI signal decay. On the other hand, the position $x = 0$ is advantageous because the target is surrounded by sensors and therefore data carry information from multiple views around the targets. At $x = 100$ cm, however, the target is at the edge of the instrument and not immediately under a receiver. The amount of quality data is therefore limited in this case: multi-looks around

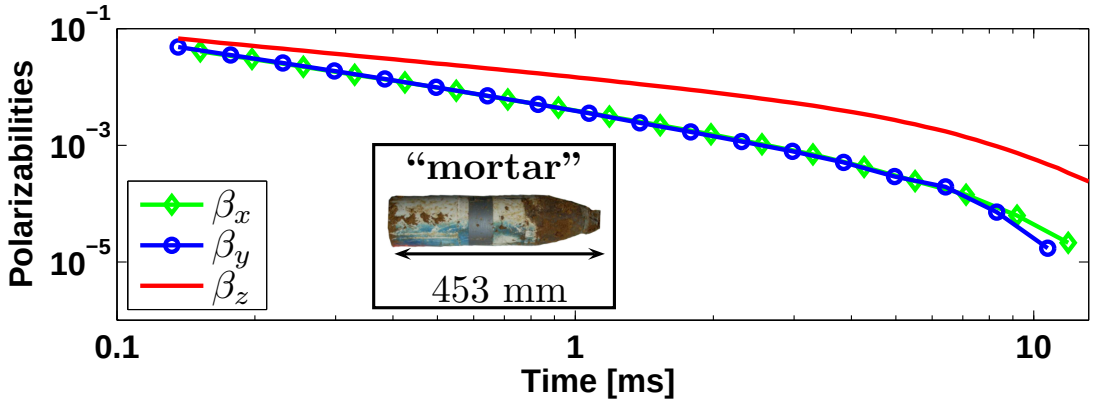

(a) Mortar. Inverted positions: (-0.5,0.6,-60.8) [cm]. True positions: (0,0,60) [cm].

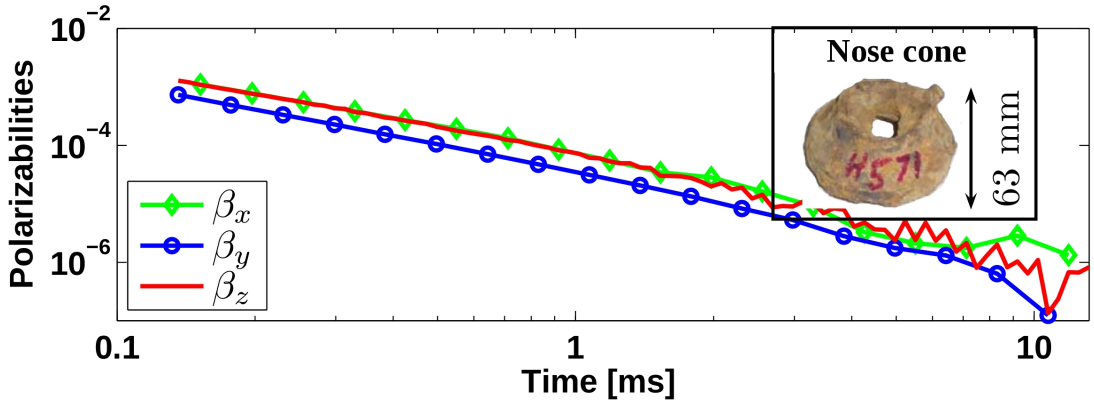

(b) Nose cone. Inverted positions: (0.2,0.2,-30.2) [cm]. True positions: (0,0,30) [cm].

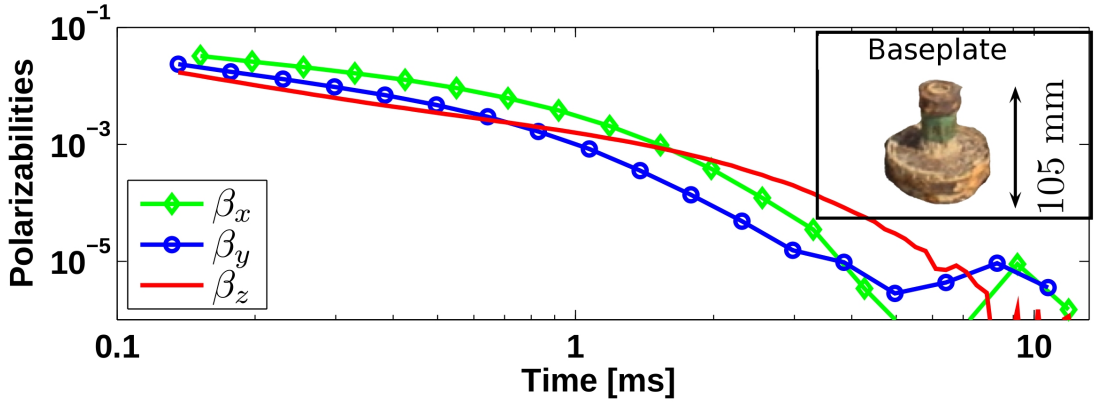

(c) Baseplate. Inverted positions: (0.4,0.1,-47.6) [cm]. True positions: (0,0,49) [cm].

Figure 7: Time domain polarizabilities and inverted positions for three independent UXO using TEMTADS data.

the target are not available and many receivers are too far away to retain usable information. As a result, inversion results are expected to be best away from the two extreme positions $x = 0$ and $x = 100$ cm.

A systematic inversion of all 11 configurations was carried out on both sets of measurements (mortar + nose cone and mortar + baseplate). The inverted positions for the first set are listed in Table 5 and the time signatures are shown in Figure 8(a). The results show polarizabilities of the mortar practically identical for all 11 configurations, as expected since the polarizabilities $\overline{\overline{\beta}}$ are an intrinsic property of the target, independent of its location and orientation. The polarizabilities of the nose cone present more variations, primarily due to the fact that some configurations correspond to a nose cone located close to either $x = 0$ and $x = 100$ cm. Nonetheless, all the signatures are seen to be linear and in good relationship with one another. The inverted positions of both targets remain within ± 1 cm accuracy for x between 20 cm and 60 cm, except for the depth of the nose cone whose error can amount to a few centimeters. The largest error, of about 9 cm, corresponds to the case when the lateral offset is $x = 100$ cm which brings the target at the edge of the instrument.

The results for the second set of measurements (mortar + baseplate), summarized in Table 6 and Figure 8(b), present more variations between the 11 configurations (note that the polarizabilities of the baseplate have been scaled by 10^{-2} in order to separate them from those of the mortar). The signature of the mortar, although still clearly separated into a strong component and two smaller identical ones, exhibits more fluctuations than in the previous case but not substantial enough to hinder a proper identification of this target. The polarizabilities of the baseplate also show a flipping dipole behavior between $\hat{x}$ in early time and $\hat{z}$ in late time, albeit somewhat smoothed out in the fluctuations between all the 11 configurations. Note again that fluctuations in the signature of the second object are expected due to its varying position which reaches the extremity of the sensor in some cases.

A series of eleven three-target configurations were analyzed whereby two targets were fixed and one was moving from case to case. The stationary targets were the mortar held horizontally at $(x,y,z) = (0,0,60)$ [cm] and the baseplate held horizontally at $(x,y,z) = (50,0,49)$ [cm]. The moving target was the nose cone held vertically at $(x,y,z) = (dx,0,30)$ [cm] with dx varying from 0 to 100 cm in increments of 10 cm. The recovered positions for these configurations are summarized in Table 7 and show an overall good agreement with the ground truth. The two

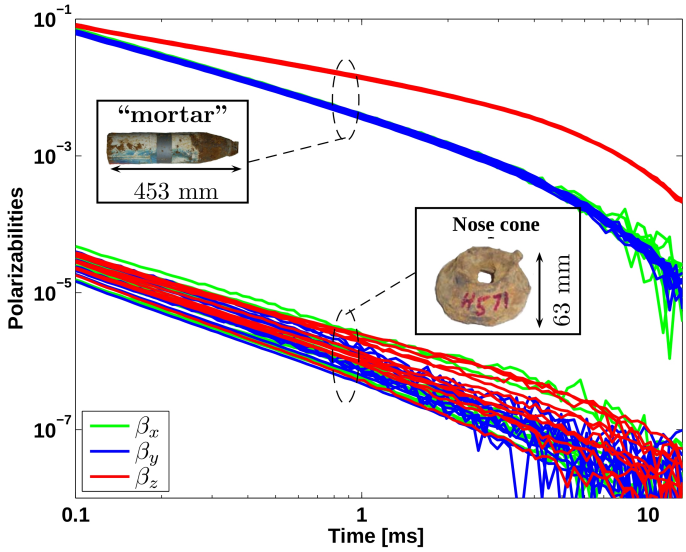

(a) Mortar + Nose cone.

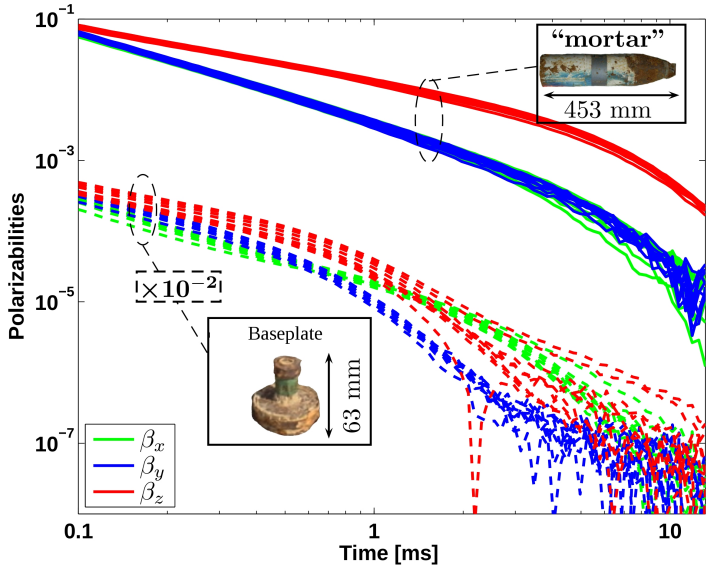

(b) Mortar + Baseplate.

Figure 8: Time dependent polarizabilities for two-target inversions from TEMTADS data. The various cases correspond to various lateral displacements along $\hat{x}$ of the shallower target while the deeper one (the mortar) is kept at a constant location. True and inverted positions are given in Table 5 and Table 6. Note that the polarizabilities of the baseplate in (b) have been scaled by 10^{-2} in order to visually separate them from those of the mortar.

	Mortar			Baseplate			
	x	y	z		x	y	z
Truth	0	0	60	dx		0	30
Case							
1	-1	1	62	0	2	0	33
2	0	1	60	10	15	0	30
3	1	1	61	20	21	0	34
4	1	1	61	30	31	0	34
5	1	1	60	40	41	-1	34
6	0	1	61	50	51	0	32
7	1	1	60	60	60	0	33
8	0	1	60	70	67	0	31
9	0	1	60	80	75	0	31
10	0	1	60	90	79	0	33
11	0	1	60	100	80	0	39

Table 5: True and inverted positions of two simultaneous targets whose time dependent polarizabilities are shown in Figure 8(a) (TEMTADS data). Ground truth corresponds to a fixed mortar and a moving nose cone along the $\hat{x}$ axis by the indicated dx while keeping y and z constants. Deviations of the first few cases are due to the difficulty in inverting accurate positions when the two targets are on top of each other whereas deviations of the last few cases are explained by the fact that the target location extends beyond the physical size of the sensor. All dimensions are in centimeters and positions are rounded to the closest integer.

stationary targets are well located in the (xy) plane and the depths are typically estimated within a centimeter for the mortar and within a couple of centimeters for the baseplate, except again in a few isolated cases that correspond for the most part to targets at the edge of the instrument. The positions of the nose cone present more fluctuations while still following the ground truth reasonably well in the majority of cases. The most problematic positions are still those corresponding to the target being at the limit of the field of view of the instrument where an error up to 9 cm in lateral position and 8 cm in depth is recorded. The time-dependent polarizabilities, shown in Figure 9, confirm these conclusions. The mortar as well as the baseplate present very consistent signatures from case to case. Interestingly, the signatures of the baseplate are more consistent than in the two-target inversions of Figure 8(b), primarily due to the larger lateral separation with the mortar (50 cm in this case). The polarizabilities of the nose cone are a few orders of magnitude lower than those of the mortar and baseplate, but with much more variations from case to case. We again attribute these to two main reasons: overlapping targets and edge effects. Edge effects refer to the effect already witnessed, by which the

	Mortar			Baseplate			
	x	y	z		x	y	z
Truth	0	0	60	dx		0	49
Case							
1	-4	1	53	0	-14	3	44
2	10	1	58	10	11	1	48
3	-1	1	56	20	26	1	47
4	1	1	58	30	32	1	48
5	1	0	59	40	41	1	48
6	1	0	59	50	50	0	48
7	1	0	60	60	59	0	47
8	1	0	60	70	67	0	47
9	1	0	60	80	73	0	47
10	0	0	60	90	80	0	49
11	0	0	60	100	89	0	51

Table 6: True and inverted positions of two simultaneous targets whose time dependent polarizabilities are shown in Figure 8(b) (TEMTADS data). The ground truth corresponds to a fixed mortar and a moving baseplate along the $\hat{x}$ axis by the indicated dx while keeping y and z constants. Deviations of the first few cases are due to the difficulty in inverting accurate positions when the two targets are on top of each other whereas deviations of the last few cases are explained by the fact that the target location extends beyond the physical size of the sensor. All dimensions are in centimeters and positions are rounded to the closest integer.

inverted position and time domain polarizabilities of a target located at the edge of the instrument can present large errors. It is therefore expected that the region close to $x = 100$ cm is a source of inaccurate polarizabilities. The overlapping target effect refers to the fact that EMI signatures are intrinsically challenging to separate for targets in proximity and on top of each other. In this particular set of measurements, the nose cone travels from $x = 0$ to $x = 100$ cm and is directly on top of targets at $x = 0$ (the mortar) and $x = 50$ cm (the baseplate). A case by case examination reveals that the position $x = 0$ is well inverted and that the polarizabilities exhibit the expected linear decay (on a log-log scale) visible for example in Figure 8(a). The polarizabilities when the nose-cone is close to $x = 50$ cm, however, present much more variation and can be seen in Figure 9(a). The major difference between the two situations are the distances between the targets when they coincide laterally: 30 cm in one case and about 20 cm in the other. It is expected that diversification of the positions by allowing for variations in the $\hat{y}$ direction would significantly improve the results. Note also that in all cases, including those challenging ones, the inverted positions remain within reasonable

	Mortar			Baseplate			Nose cone			
	x	y	z	x	y	z		x	y	z
Truth	0	0	60	50	0	49	dx		0	30
Case										
1	2	0	61	50	0	47	0	0	0	36
2	2	1	58	50	0	47	10	14	0	31
3	2	0	59	50	0	47	20	22	1	31
4	2	1	59	51	0	47	30	28	1	34
5	2	1	60	55	1	47	40	37	1	36
6	1	1	59	50	1	49	50	49	0	38
7	3	1	59	42	1	50	60	58	0	36
8	1	1	59	50	0	46	70	81	3	27
9	2	1	59	48	1	48	80	84	0	32
10	2	1	59	47	0	48	90	83	0	38
11	2	1	60	55	0	43	100	-	-	-

Table 7: True and inverted positions of three simultaneous targets whose time dependent polarizabilities are shown in Figure 9 (TEMTADS data). The ground truth corresponds to a fixed mortar, a fixed baseplate, and a moving nosecone along the $\hat{x}$ axis by the indicated dx while keeping y and z constants. All dimensions are in centimeters and positions are rounded to the closest integer.

bounds.

4.2.e Discussion and Conclusions

The Gauss-Newton based algorithm presented in this paper has been shown to be effective at simultaneously inverting for the positions, orientations, and time dependent polarizabilities of multiple UXO within the field of view of EMI sensors. Part of the efficiency is due to the construction of the unknown vector, in which positions and orientations of the targets' equivalent dipoles are assumed time independent and inverted for only once using the information of all time channels. Another important aspect of the algorithm is that it is largely based on an analytical derivation of the Jacobian matrix, which therefore provides exact derivatives of the secondary magnetic field with respect to all unknown quantities while reducing the computation time.

Inherent to the method itself, various initial guesses to seed the algorithm and maximum iterations numbers have been tested, depending on the complexity of the cases studied. For single targets, 10 iterations were in general sufficient whereas up to 200 iterations were run for three-target cases. An increased number of iterations naturally results in an increased computation time, which reached almost

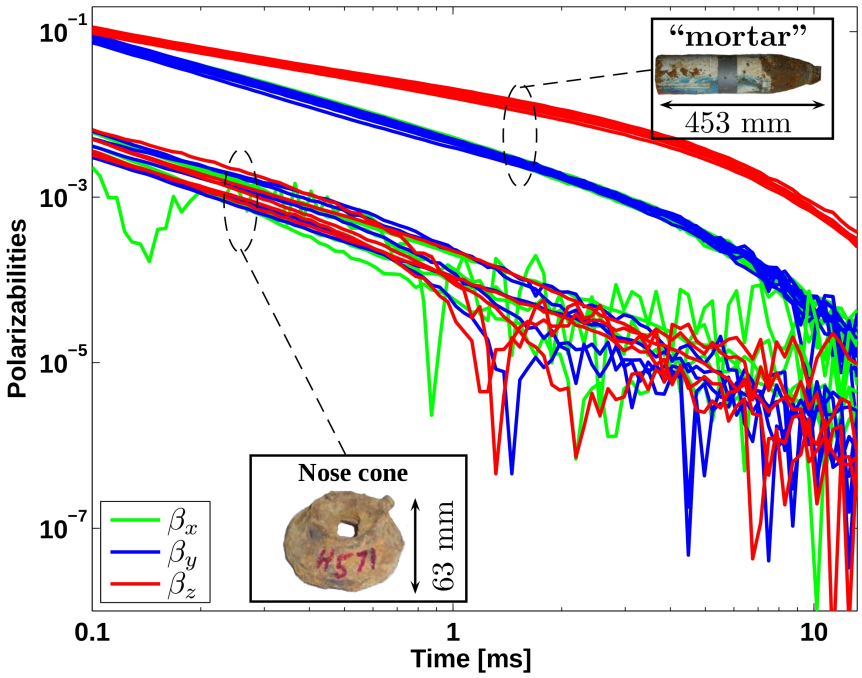

(a) Mortar and nose-cone.

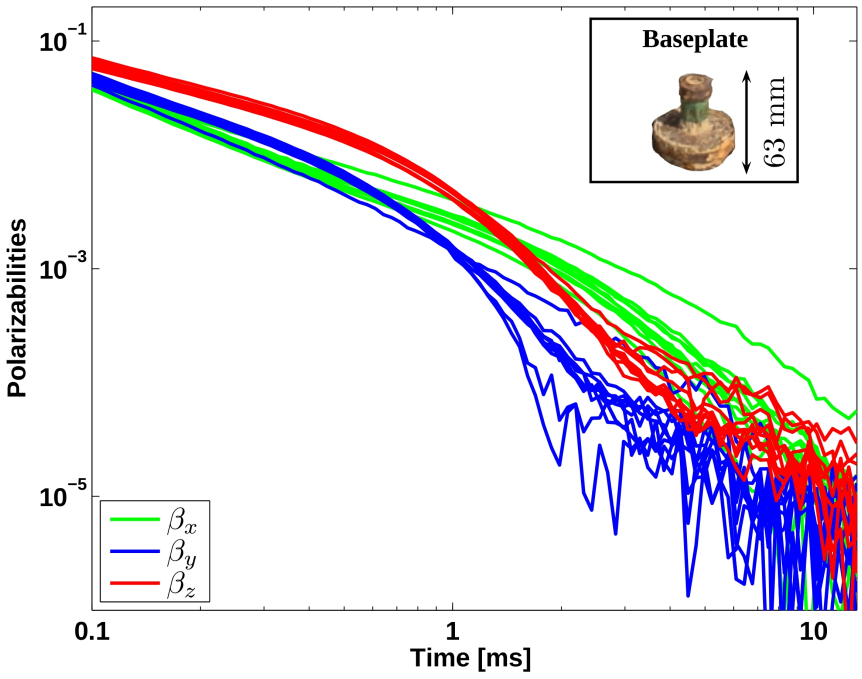

(b) Baseplate.

Figure 9: Three-target inversions from TEMTADS data. The mortar and the baseplate are held fixed at $(x,y,z) = (0,0,60)$ [cm] and $(x,y,z) = (50,0,49)$ [cm], respectively, while the nose-cone moves along $\hat{x}$ from case to case. True and inverted positions are given in Table 7.

3 minutes in case of TEMTADS data inverted on three targets (we recall that the TEMTADS data set is typically much larger than the MPV data set so that inversions are more time consuming). The final solution produced by the algorithm is remarkably insensitive to the initial guess (apart from obvious divergences), provided that the step at each iteration is weighted by a parameter $0 < \alpha < 1$. A value of $\alpha = 0.5$ yielded very consistent inverted positions in all examples shown despite large variations in initial guesses: within ± 50 cm for both x and y coordinates and between -50 cm and -20 cm for the depths. The inverted polarizabilities, however, were more sensitive especially in the three-target cases, yet still within acceptable bounds. To resolve possible variations, the algorithm was run on typically 10 realizations. The selection of the final solution was performed by using two often corroborating criteria. First, the histogram of solutions for the inverted positions was examined and the most frequent solution was declared final. Second, the error was computed between the measured field and the computed field and the solution that produced the lowest error was declared final. In all cases considered these two criteria selected identical solutions. It should also be mentioned that simpler cases such as single target inversion yielded similar final solutions in almost all the cases, so that the criteria proposed above were mostly useful when inverting multi-target configurations.

Finally, we emphasize that the assumption of a known number of targets (i.e. known N in Eq. (4.4)) is necessary for the development of the algorithm but is not required in practice and only the knowledge of an upper bound is needed. If the algorithm is run with N larger than the actual number of targets, the algorithm may yield two types of results. First, some dipoles cluster around a certain location and capture the secondary field of a given UXO better than a single dipole. This situation is not very common but can occur for very heterogeneous targets. More commonly, clusters are very tight and the dipoles find themselves practically at the same location. The corresponding time-dependent polarizabilities need to be added and collectively represent the signature of the target (individual polarizabilities typically do not exhibit any physical behavior). The second type of results obtained if N is larger than the actual number of targets is that some dipoles converge to apparently irrelevant locations, with polarizabilities a few orders of magnitude lower than those of the targets themselves. We attribute this behavior to the algorithm's attempt to find a best fit for noisy data, which is obtained with a few well-identified dipoles and other weaker ones that capture average noise contributions. At the target identification stage, these spurious dipoles are easily

filtered out due to their unphysical and weak responses. Note also that this latter behavior prevents the use of the misfit error to determine the number of targets since smaller errors are typically obtained with more dipoles. Consequently, the algorithm does not require the exact knowledge of the number of targets for their proper identification, and only an upper bound needs to be estimated. This topic is currently under investigation.

4.3 Joint Diagonalization and the Orthonormalized Volume Magnetic Source Methods

We apply a volume dipole distribution model to next-generation sensor data for multi-object data inversion and discrimination. Discrimination between UXO and harmless objects is particularly difficult in highly contaminated sites where two or more objects are simultaneously present in the field of view of the sensor and produce overlapping signals. The first step in overcoming this problem is estimating the number of targets. In this report an orthonormalized volume magnetic source (ONVMS) approach is introduced for estimating the number of targets, along with their locations and orientations. The technique is based on the discrete dipole approximation, which distributes dipoles inside the computational volume. First, a set of orthogonal functions are constructed using fundamental solutions of the Helmholtz equation (*i.e.*, Green's functions). Then, the scattered magnetic field is approximated as a summation of these orthogonal functions. The magnitudes of the expansion coefficients are determined directly from the measurement data without solving an ill-posed inverse-scattering problem. The expansion coefficients are then used to determine the amplitudes of the responding volume magnetic dipoles. The algorithm's superior performance and applicability to live UXO sites are illustrated by applying it to the bi-static TEMTADS multi-target data sets collected by NRL personnel at the Aberdeen Proving Ground UXO test-stand site.

4.3.a Introduction

Remediation of lands contaminated with unexploded ordnance (UXO) at Department of Defense and Department of Energy sites has been identified as one of the military's most pressing environmental problems [50]. As a result of past military and weapon-testing activities, UXO are found at both active and formerly used defense sites (FUDS) (closed, transferred and transferring ranges, munitions burning and open detonation areas). In the United States alone, more than 900 sites, about

11 million acres of land, are potentially contaminated with UXO. The costs of excavating all geophysical anomalies are well-known and are one of the greatest impediments to the efficient cleanup of UXO, particularly at highly contaminated UXO sites, where multiple objects are often present simultaneously in the sensors' field of view. State-of-the-art electromagnetic induction (EMI) sensors have recently emerged as the most cost-effective sensing technology for detecting and discriminating between UXO and non-hazardous items. These sensors are easy to operate in various environments and can be deployed hand-held or on a variety of mobile platforms. For the low frequencies and high conductivities of interest here, induced conduction currents are much stronger than displacement currents, so the latter can usually be neglected in both target and the surrounding soil. In this frequency regime, electric fields are typically quite small, and the conductivity of the surrounding soil is typically many orders of magnitude less than that of the metallic target. Together with the low frequency range, this means that the dielectric properties of the surrounding media are negligible and could be treated as free space, which makes EMI sensors more attractive when compared to electromagnetic wave sensing technologies.

In current practice, most EMI sensors are composed of separate transmitting and receiving coils. When the operator activates the sensor, a current runs through the transmitter coils, which results in the establishment of a ("primary" or "principal") magnetic field in the surrounding space. By Faraday's law, this time-varying magnetic field induces eddy currents in highly conducting bodies; ferromagnetic bodies also have their magnetization affected by the impinging field. These currents and magnetization in turn generate a ("secondary" or "scattered") magnetic field that also varies with time and induces measurable currents in the receiving coils. At the end, the electromagnetic data are inverted using different forward models.

Recently, several EMI sensing and data-inversion techniques [4, 20, 24, 50–64] have been developed for detecting and discriminating between UXO and non-UXO items. Typically the first step of these methods is the recovery of a set of parameters that specify a physics-based model representing the object under interrogation. For example, in EMI sensing, the recovered parameters consist of the object's location and spatial orientation in addition to "intrinsic" parameters such as the polarizability tensor (along with some parametrization of its time-decay curve) in dipole models or the amplitudes of responding magnetic sources in the NSMS and SEA models. EMI responses depend nonlinearly on

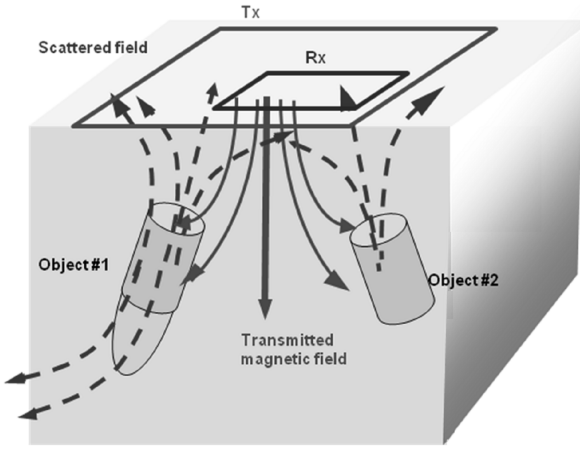

Figure 10: Metallic objects under the transmitter. The target's EMI response at the receiver coil can be calculated from the volume magnetic dipole moment $d\mathbf{m}$.

the subsurface object's location and orientation, and therefore the determination of a buried object's orientation and location is a non-linear problem. In the last decade several inverse scattering approaches have been adapted for EMI data inversion [52, 53, 55, 65, 66]. These algorithms are carried out by determining an objective function as a goodness-of-fit measure between the forward model and measurement data.

Although various forward EMI models (such as single-dipole, multi-dipole [20, 50–53], and normalized surface magnetic source [4, 24]) have demonstrated great UXO discrimination capabilities for well-isolated single targets using data provided by next-generation EMI sensors, single-target discrimination capability is considerably limited for overlapping EMI signals; *i.e.*, when a sensor detects EMI signals from two or more targets at the same time. The obvious extension of current EMI modeling to accommodate overlapping EMI signatures is multiple-target modeling. However, when we apply multi-target modeling to real data, the accuracy of the solution is generally limited by the ill-posed nature of the inverse problem and, thus, multi-target modeling with more than two targets is seldom applied in practice in UXO detection and discrimination.

Even when multi-target EMI forward modeling is applied to high-fidelity next-generation sensor EMI data, the first step is estimating the number of targets and then extracting the intrinsic parameters of these multiple targets, which generally requires a highly multidimensional linear and nonlinear optimization search. In many cases, extracting linear parameters from a limited set of data is an ill-posed problem with many solutions and for which no existing technique can guarantee

that the true solution will be attained within the practical limits of computational time. Therefore, the success of multiple-target parameter estimation greatly depends on how closely a forward model with a small number of model parameters can take into account the underlying physics of EMI scattering phenomena. One way to incorporate the physics faithfully is to apply the orthonormalized volume magnetic source (ONVMS) model to the multi-object UXO discrimination problem. The algorithm is based on the discrete interacting dipole approximation and represents EMI scattered fields using a set of orthogonal functions. This paper combines the ONVMS with a global search technique called differential evolution [65, 66] to determine target locations and orientation starting from next-generation sensor data. It then uses joint diagonalization [67] to estimate the number of contributing targets and to de-noise signals.

The paper is organized as follows: Sec. 4.3.b presents the orthonormalized volume magnetic source technique, Sec. 4.3.c describes orthonormalized functions, and Sec. 4.3.d presents the joint diagonalization approach. Section 4.3.e shows experimental and numerical results that demonstrate the applicability of the combined ONVMS-DE algorithm and joint diagonalization approach to the detection and discrimination of multiple buried objects starting from actual EMI data collected by the TEMTADS array.

4.3.b The Orthonormalized Volume Magnetic Source Mode

Let us consider permeable and highly conducting metallic 3-D objects placed in a time varying primary magnetic field (see Fig. 10). As is well established in the EMI frequency regime, we assume that displacement currents $\partial D/\partial t$ are negligible. Further, the conductivity of the soil and the electric fields within it are small and combine to produce negligible currents. The primary magnetic field penetrates the object to some degree, inducing eddy currents/magnetic-dipoles inside it. In return, these induced sources produce a secondary or scattered magnetic field outside the objects that can be represented as a sum of magnetic fields due to a normalized set of magnetic sources distributed over a volume:

$$\mathbf{H}^{sc}(\mathbf{r},p) = \int_V \frac{1}{4\pi\mu_0 R^3}\mathbf{m}(\mathbf{r'}_v,p)\cdot(3\hat{\mathbf{R}}\hat{\mathbf{R}}-\bar{\bar{\mathbf{I}}})dv' \tag{4.14}$$

where $p = t, f$ is time or frequency, $\hat{\mathbf{R}}$ is the unit vector along $\mathbf{R} = \mathbf{r} - \mathbf{r'}_v$, $\mathbf{r'}_v$ is the position of the v'-th infinitesimal dipole in the volume V, $\mathbf{r}$ is the observation

point (see Fig. 10), and $\bar{\bar{\mathbf{I}}}$ is the identity dyad. In the ONVMS approach the induced magnetic dipole moment $\mathbf{m}(\mathbf{r}_{v'}, p)$ at point $\mathbf{r}_{v'}$ on the surface is related to the primary field via $\mathbf{m}(\mathbf{r}_{v'}, p) = \bar{\bar{\mathbf{M}}}(\mathbf{r}_{v'}, p) \cdot \mathbf{H}^{pr}(\mathbf{r}_{v'})$, where $\bar{\bar{\mathbf{M}}}(\mathbf{r}_{v'}, p)$ is the symmetric polarizability tensor. Overall, in the NVMS approach the scattered magnetic field is approximated as a superposition of the fields radiated by these elementary sources, whose amplitudes are normalized with the impinging primary magnetic field $\mathbf{H}^{pr}$. According to a simplification of the elementary atomic model of matter, all materials are composed of atoms, each with a positively charged nucleus and a number of orbiting negatively charged electrons. The orbiting electrons cause circulating currents and form microscopic magnetic dipoles inside the targets. In the absence of an external magnetic field the magnetic dipoles of atoms of most materials have random orientations, resulting in no magnetic moment. The application of an external time-varying magnetic field, by Faraday's law, induces eddy currents in highly conducting bodies by an alignment of the magnetic moments of the spinning electrons and a magnetic moment due to a change in the orbital motion of electrons. These currents and magnetization in turn generate a ("secondary" or "scattered") magnetic field that also varies with time and induces measurable currents in the receiving coils. Since the induced magnetic dipoles/eddy currents are distributed inside the object, the spatial distribution of the magnitudes of the dipoles indicate the locations and orientations of any targets present inside the volume. The equation (4.14) in discrete form can be written as

$$\mathbf{H}(\mathbf{r}) = \sum_{i=1}^{N_v} \frac{1}{4\pi\mu_0 R_i^3} (3\hat{\mathbf{R}}_i\hat{\mathbf{R}}_i - \bar{\bar{\mathbf{I}}}) \cdot m_i \equiv \sum_{i=1}^{N_v} \bar{\bar{G}}_i(\mathbf{r}) \cdot m_i, \tag{4.15}$$

where $\bar{\bar{G}}_i(\mathbf{r})$ is Green's dyad.

4.3.c Orthonormalized Functions

The scattered magnetic field at any point outside the volume (4.14) can be represented using orthonormalized functions as

$$\mathbf{H}(\mathbf{r}) = \sum_{i=1}^{N_v} \bar{\bar{\psi}}_i(R_i) \cdot b_i, \tag{4.16}$$

where $\mathbf{R}_i = \mathbf{r} - \mathbf{r}_i^v$, $\{\mathbf{r}_i^v\}_{i=1}^N \in V$, $\bar{\bar{\psi}}_i(\mathbf{r})$ is an orthonormalized function, and b_i is orthogonal-function expansion coefficient. The orthonormalized functions $\bar{\bar{\psi}}_i(\mathbf{R}_i)$

are linearly independent at the observation point:

$$\sum_{n=1}^{M} \bar{\bar{\psi}}_n \cdot \mathbf{c}_n = 0. \tag{4.17}$$

This means that all coefficients $\boldsymbol{c}_1 = \boldsymbol{c}_2 = \ldots = \boldsymbol{c}_M = 0$. In addition, the set of orthogonal functions is complete, which guarantees that there is a set of coefficients $\mathbf{c}_n$, $n = 1,\ldots,M$, that will specify the magnetic field $\mathbf{H}$ at any point with arbitrary-εg accuracy:

$$\sqrt{\int \left| \mathbf{H} - \sum_{n=1}^{M} \bar{\bar{\psi}}_n \cdot \mathbf{C}_n \right|^2 ds} < \varepsilon, where \varepsilon \ll 1.$$

The orthonormal functions $\bar{\bar{\psi}}_n$are constructed as linear combinations of the Green's functions using the Gram–Schmidt orthonormalization process,

$$\bar{\bar{\psi}}_m = \bar{\bar{G}}_m - \sum_{k=1}^{m-1} \bar{\bar{\psi}}_k \cdot \bar{\bar{A}}_{mk}, \tag{4.18}$$

where $\bar{\bar{G}}_m$ is Green's dyad from (4.15) and the tensor $\bar{\bar{A}}_{mk}$is determined as

$$\bar{\bar{A}}_{mn} = \bar{\bar{F}}_n^{-1} \left(\bar{\bar{C}}_{nm} - \sum_{k=1}^{n-1} \bar{\bar{A}}_{nk}^T \cdot \bar{\bar{F}}_k \cdot \bar{\bar{A}}_{mk} \right), \quad (\bar{\bar{A}}_{mn} = 0,\ m \le n) \quad . \tag{4.19}$$

The functions $\bar{\bar{\psi}}_k$satisfy the orthogonality conditions

$$\int \left(\bar{\bar{\psi}}_m^T \cdot \bar{\bar{\psi}}_k \right) dv = \begin{cases} \bar{\bar{0}}, & m \neq k \\ \bar{\bar{F}}_m, & m = k \end{cases} \tag{4.20}$$

and

$$\int \left(\bar{\bar{G}}_m^T \cdot \bar{\bar{G}}_k \right) dv = \bar{\bar{C}}_{mk}. \tag{4.21}$$

The orthogonal functions expansion coefficients b_i in equation (4.16) can be determined from actual data $\mathbf{H}^{data}$ using the orthogonality property of the $\bar{\bar{\psi}}$ given in (4.20):

$$b_i = \bar{\bar{F}}_i^{-1} \cdot \int \bar{\bar{\psi}}_i^T \cdot \mathbf{H}^{data}\, dv. \tag{4.22}$$

In addition, (4.18) can be rewritten as

$$\bar{\bar{\psi}}_i(s) = \sum_{n=1}^{i} \bar{\bar{G}}_n(s) \cdot \bar{\bar{B}}_{in}, \tag{4.23}$$

where the tensor coefficient $\bar{\bar{B}}_{in}$ can be determined using the tensors $\bar{\bar{A}}_{ni}$ from (4.19) through

$$\bar{\bar{B}}_{\substack{mi \\ m>2 \\ i\le m}} = -\sum_{n=1}^{m} \bar{\bar{A}}_{ni}\cdot\bar{\bar{B}}_{mn},\ \ \bar{\bar{B}}_{mm}=\bar{\bar{I}},\ \ \bar{\bar{B}}_{m(m-1)}=\bar{\bar{A}}_{m(m-1)}. \tag{4.24}$$

Finally, by combining (4.16) and (4.23), the scattered magnetic field can be expressed as

$$\mathbf{H}(\mathbf{r})=\sum_{i=1}^{N_v}\bar{\bar{\psi}}_i(s)\cdot b_i=\sum_{i=1}^{N_v}\sum_{n=1}^{i}\bar{\bar{G}}_n(\mathbf{r})\cdot\bar{\bar{B}}_{in}\cdot b_i=\sum_{i=1}^{i}\bar{\bar{G}}_i(\mathbf{r})\cdot\left(\sum_{n=1}^{m}\bar{\bar{B}}_{in}\cdot b_n\right)=\sum_{i=1}^{N_v}\bar{\bar{G}}_i(\mathbf{r})\cdot m_i, \tag{4.25}$$

and comparing (4.15) to (4.25) and using the linear independence of Green's functions one can conclude that

$$\mathbf{m}_i=\sum_{n=1}^{i}\bar{\bar{B}}_{in}\cdot b_i.$$

Thus the amplitudes of the responding magnetic dipoles are determined without solving a linear system of equations.

4.3.d Joint Diagonalization

Recently, under the Strategic Environmental Research and Development Program (SERDP), next generation EMI sensors have been developed for discriminating between subsurface UXO and clutter. One such sensor is the Time domain Electromagnetic Multi-Sensor Towed Array Detection Systems (TEMTADS).The system consists of 25 transmit/receive pairs of square coil antennas arranged in a 5×5 grid, each consisting of a 35-cm transmitter loop and a 25-cm receiver loop. The sensor activates the transmitter loops in sequence, one at a time, and for each transmitter all receivers receive, measuring the complete transient response over a wide dynamic range of time: from approximately 100 μs to 25 ms distributed in 123 time gates. The sensor thus provides 625 spatial data points at each instrument location, offering unprecedented positional accuracy. Recent TEMTADS blind discrimination studies [24] show perfect performance when the number of targets was known a priori. However, determining the number of potential targets and locating them is still a challenging problem. To take advantage of the high fidelity data provided by TEMTADS, here we employ the joint diagonalization algorithm

to estimate the number of targets directly from the data using eigenvalues. Let us briefly describe the joint diagonalization algorithm for the TEMTADS system. For a given time channel t_q, $q = 1, 2, \ldots, N_q$, where N_q is the number of time channels, let us define $H_{k.m}$ as the z-component of the magnetic field measured by the m-th receiver coil when the k-th transmitter is active, and the matrix

$$\bar{\bar{H}}(t_q) = \begin{bmatrix} H_{1,1} & H_{1,2} & \cdots & H_{1,M} \\ H_{2,1} & H_{2,2} & \cdots & H_{2,M} \\ \vdots & \vdots & \ddots & \vdots \\ H_{K,1} & H_{K,2} & \cdots & H_{K.M} \end{bmatrix} \tag{4.26}$$

as a set of measured data/vector for the k-th transmitter, where $k = 1, 2, \ldots, K$.

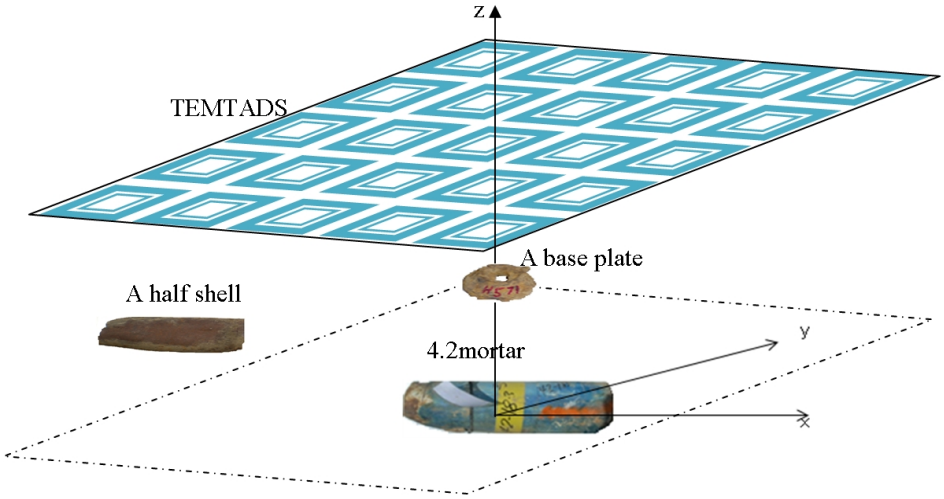

Figure 11: A schematic diagram of the three-target TEMTADS experimental setup. The targets are: 1) 4.2" mortar oriented horizontally along the x axis and placed at (x=y=0) 60 cm bellow the TEMTADS centerline; 2) A half-shell oriented horizontally, placed at x=–50 cm, y=0, and 47 cm bellow the TEMTADS; 3) A base plate oriented vertically, placed at x=y=0, and 27 cm bellow the TEMTADS. The TEMTADS center is at x=y=0; z=60 cm.

For the TEMTADS system $M = 25$ is the number of receivers and $K = 25$ is the number of transmitters. For each time channel the $M \times K$ matrix $[H^d]$ can be expressed with eigenvectors $U(t_q)$ and eigenvalues $D(t_q)$ using the singular value decomposition:

$$\bar{\bar{H}}(t_q) = \bar{\bar{U}}(t_q)\bar{\bar{D}}(t_q)\bar{\bar{U}}^T(t_q). \tag{4.27}$$

However, in order to determine the number of potential targets, we need to find an eigenvector V that will be shared by all $\left\{\bar{\bar{H}}^d(t_q)\right\}_{q=1}^{N_q}$ matrices and will also make vanish all off-diagonal elements of the matrix

$$\bar{\bar{D}}(t_q) = \bar{\bar{V}}^T \bar{\bar{H}}(t_q)\bar{\bar{V}}, \quad q = 1 \text{ to } N_q. \tag{4.28}$$

In general, it is not the case that V will cancel all off-diagonal elements of $\bar{\bar{D}}(t_q)$. The technique that finds a unitary $\bar{\bar{V}}$ matrix that minimizes the $\left\{\bar{\bar{H}}^d(t_q)\right\}_{q=1}^{N_q}$ matrices' off-diagonal elements is called the joint diagonalization approach [67].

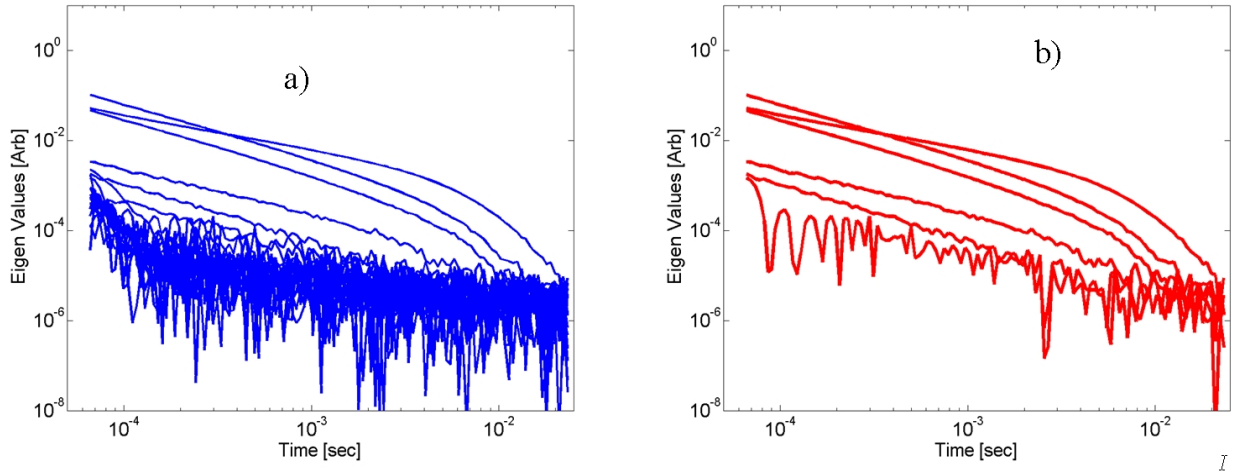

Figure 12: Eigenvalues versus time for 4.2" mortar TEMTADS data: a) All 25 eigenvalues. b) The three highest eigenvalues are associated with the 4.2" mortar and the next three correspond to non dipole terms.

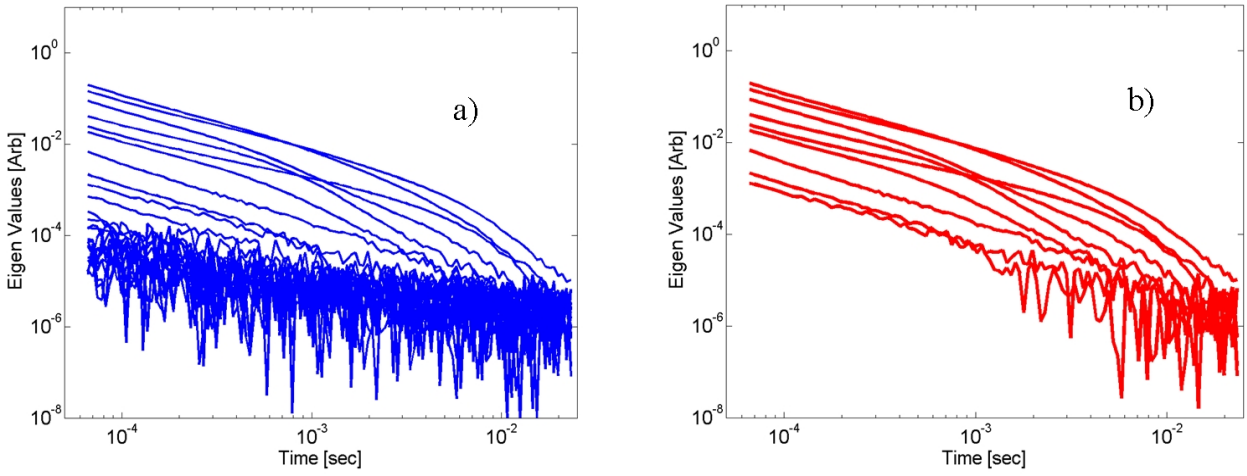

Figure 13: Eigenvalues versus time for three-target TEMTADS data: b) All 25 eigenvalues. b) The first three highest eigenvalues are associated with 4.2" mortar, half shell and base plates.

4.3.e Results

First we apply the joint diagonalization model to measured 4.2" mortar TEMTADS data collected over a calibration test stand. The object was placed horizontally at a 60 cm depth under the TEMTADS array centerline. The $\bar{\bar{H}}(t_q)$ data were diagonalized using (4.28). Figure 12(a) shows all 25 eigenvalues vs. time for the TEMTADS magnetic field $\bar{\bar{H}}(t_q)$. The result shows that there are three strong eigenvalues and that the rest are small. Since the data was taken only for one 4.2" mortar, we could conclude that these strong eigenvalues correspond to the mortar and rest of the eigenvalues are associated to sensor noise. Figure 12(b) shows the eigenvalues larger than a particular threshold after smaller eigenvalues are removed.

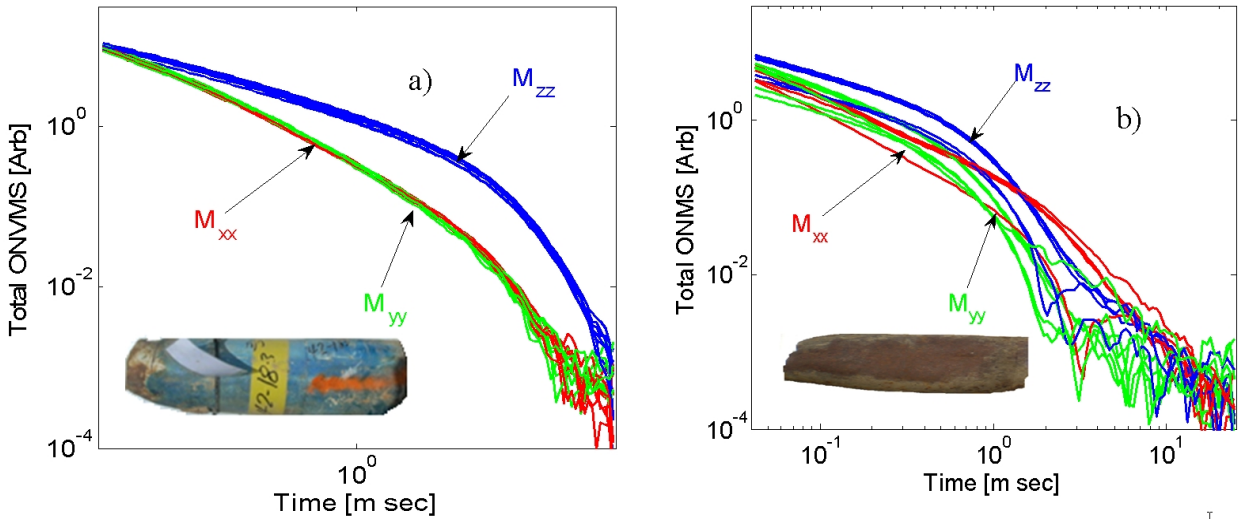

Figure 14: The total ONVMS versus time for: a) 4.2" mortar and b) half-shell inverted from three-object TEMTADS data, when base plates were placed at the six different locations shown in Table 15 below.

Next we applied the proposed approach to three-object TEMTADS data. The schematic diagram of the experimental setup is depicted on Fig. 11. The data were acquired by NRL personnel at the Blossom Point UXO test stand site. The sensor was stationary, and the 4.2" mortar was placed horizontally at 61 cm under the array centerline while the half shell was lying horizontally and placed under the array centerline at 47 cm depth, $x = -50$ cm offset, $y = 0$. The base plate was kept at 27 cm depth and moved from the center along negative x-axis at 10 cm increments while keeping $y = 0$. First we used the joint diagonalization technique to estimate the number of potential targets. Figure 13(a) shows all 25 eigenvalues vs. time for

Case #	Base plate location inverted/ actual [cm]	
	X	*Z*
1	–5/0	–27/–30
2	–12/–10	–34/–30
3	–22/–20	–35/–30
4	–35/–30	–37/–30
5	–42/–40	–37/–30
6	–54/–50	–36/–30

Figure 15: Inverted and actual locations of the base plate.

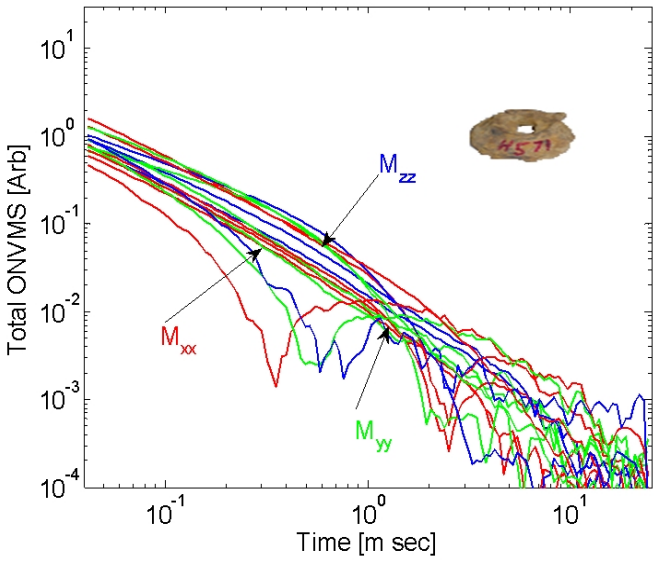

Figure 16: Inverted total ONVMS versus time for the baseplate at six different locations along the x-axis.

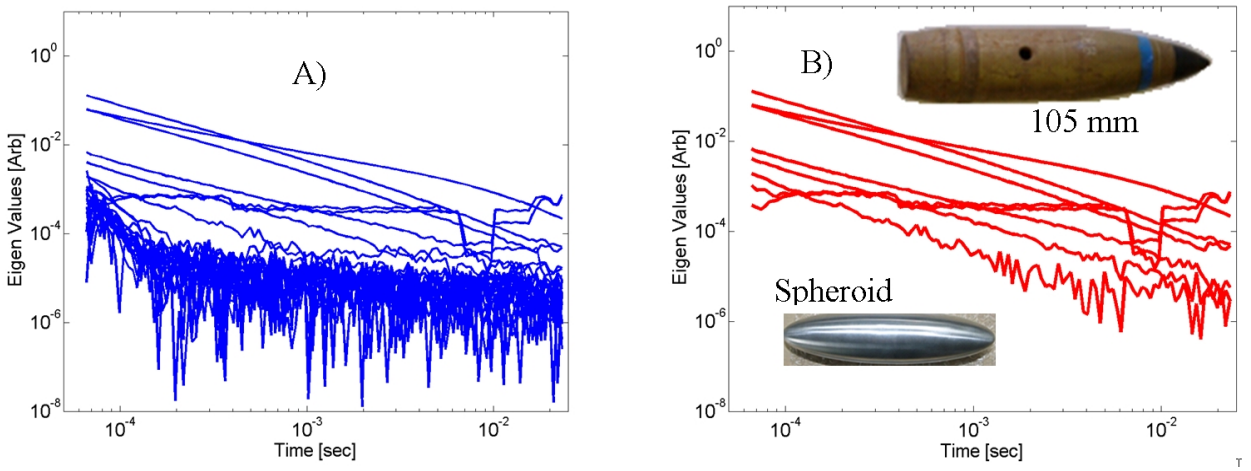

Figure 17: Eigenvalues versus time for TEMTADS data corresponding to three targets, a 105-mm projectile and two spheroids: a) All 25 eigenvalues. b) Nine highest eigenvalues.

the TEMTADS magnetic field $\bar{\bar{H}}(t_q)$ when the base plate was placed at $x = y = 0$ and the depth was 27 cm. The result shows that there are nine strong eigenvalues corresponding to the mortar, half shell, and base plates (see Figure 13(b)). The rest of the eigenvalues are small and are again associated to sensor noise, just as in Figure 12. We removed the sensor noise from the data by removing the small eigenvalues and their corresponding eigenvectors. Then we applied the combined ONVMS and differential evolution algorithm [65, 66] to the de-noised data to determine target locations and the corresponding total ONVMS in order to perform discrimination. The inverted locations of the base plates are summarized in Table 1. The results show that the algorithm inverted the small object's burial depth and location with 5-cm accuracy for all six cases. The combined ONVMS-DE algorithm also inverts the locations of the 4.2" mortar and half-shell with 3 cm accuracy for all six case (the results are not shown here).

The algorithm outputs the total ONVMS versus time for each targets. Figure 14 shows the total ONVMS for 4.2" and half-shell for all six cases. The results demonstrate that the algorithm extracts a stable total ONVMS decay curves for all three targets for the six different configurations; see Figure 14 and Figure 16. Thus the algorithm is capable to classify correctly between UXO and non-UXO items.

Finally, to demonstrate the applicability of the joint diagonalization and ONVMS-DE algorithm for a highly contaminated UXO scenario in which a big target dominates over small targets, again we employ the method on a three-target TEMTADS data set. The targets are a 105-mm projectile of length 49 cm and two

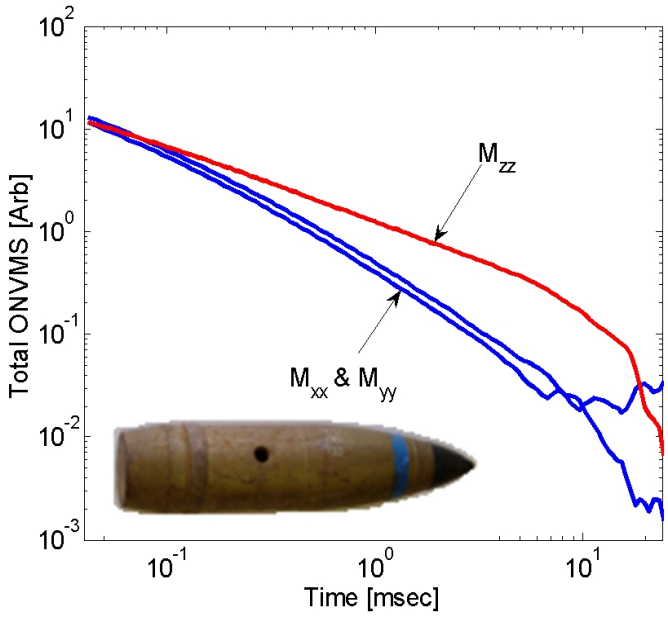

Figure 18: Inverted total ONVMS versus time for the 105 mm projectile.

steel spheroids with major to minor axis ratio $b/a = 4$ and $a = 2.5$cm. The sensor was stationary, and the 105 mm projectile was placed horizontally at 59 cm under the array centerline, while the spheroids were placed at depth 33 cm and $x = 0$, $y = 10$ cm and $x = 0$ $y = -10$ cm respectively. We apply the joint diagonalization technique to estimate the number of potential targets. Figure 17(a) shows all 25 eigenvalues vs. time for the TEMTADS magnetic field. The result shows that even when the spheroids are close to the sensor their corresponding eigenvalues are orders of magnitudes less than those of the 105-mm projectile. This indicates that the contribution from the spheroids is negligible (Fig. 17(b)). We removed the sensor noise and the spheroids' signals from the data by making all small eigenvalues and their corresponding eigenvectors be zero. Again we applied the combined ONVMS/differential evolution algorithm to the remaining, de-noised data for determining the target's location and the corresponding total ONVMS for discrimination. The algorithm correctly predicted the location. The approach inverted a stable, symmetric total ONVMS versus time for the 105-mm projectile, as shows Fig. 18.

4.3.f Conclusion

The orthonormalized volume magnetic source technique was introduced for multi-object detection and discrimination. The algorithm was applied to next-generation EMI array sensors, in particular to the TEMTADS array. The ONVMS was combined with DE to estimate target depths and locations. In addition, a joint diagonalization algorithm was adapted to TEMTADS data for estimating the number of potential targets. The TEMTADS sensor, a bi-static system with 25×25 Tx/Rx combinations, yields a 25×25 matrix for each time channel. First, by examining the eigenvalue structure of this matrix we can efficiently estimate the number of targets, and then by utilizing the combined ONVMS-DE algorithm we can locate the subsurface targets and efficiently extract their intrinsic parameters (such as the polarizability) for discrimination purposes. The accuracy of the combined technique was tested against time-domain TEMTADS data collected at calibration and test stand sites. The results show that that the combined model accurately predicts the number of targets, their burial depths and locations, andstable discrimination feature parameters that could be used to discriminate between objects of interest and non-hazardous targets.

5 Data, Results, and Discussion

5.1 TEMTADS Data and Results

The spheroids detailed in Sec. 4.1 are now all combined and in the custody of Dan Steinhurst at NOVA Research who maintains and operates the TEMTADS instrument under a contract from NRL. As part of this project, an extensive set of data was acquired over many configurations of multiple targets, including these canonical targets. Table 5.1 gives a sample of the data collected. For a full list, contact Ben Barrowes.

Data cases 117-126 were given to Dr. Fridon Shubitidze and Dr. Tomasz Grzegorczyk as a blind data set. Figure 19 shows a sample picture of the TEMTADS and the targets. Using the JD and ONVMS methods (see Sec. 4.3), he was able to correctly identify all targets in this blind data set (see Fig. 20).

Date	Prefix	Depth to Base (cm)	Targets Present	Orientation
1/15/2010	20100115_		SS1, A1	
1/15/2010	20100115_	27.5(clutter)	SS1, A1; SP4, steel	SP4S flat, along x
1/15/2010	20100115_	27.5(clutter)	SS1, A1; SP4, steel; SP4 A1	SP4S flat, along x, SP4A flat, along y
1/15/2010	20100115_	27.5(clutter)	SS1, A1; SP4, steel; SP4 A1; SP3 steel	SP4S flat, along x, SP4A flat, along y; SP3S flat, along x
1/15/2010	20100115_	27.5(clutter);63(105mm)	105mm; SS1, A1; SP4, steel; SP4 A1; SP3 steel	105mm flat, nose toward +x,SP4S flat, along x, SP4A flat, along y; SP3S flat, along x
1/15/2010	20100115_	27.5(clutter);63(105mm)	105mm; SS1, A1; SP4, steel; SP4 A1	105mm flat, nose toward +x,SP4S flat, along x, SP4A flat, along y
1/15/2010	20100115_	27.5(clutter);63(105mm)	105mm; SS1, A1; SP4, steel	105mm flat, nose toward +x,SP4S flat, along x
1/15/2010	20100115_	27.5(clutter);63(105mm)	105mm; SS1, A1	105mm flat, nose toward +x
1/15/2010	20100115_	63(105mm)	105mm	105mm flat, nose toward +x
1/15/2010	20100115_		60mm	60mm flat, nose toward +x
1/15/2010	20100115_	38(60mm)	60mm; SS1, A1	60mm flat, nose toward +x
1/15/2010	20100115_	27.5(clutter);38(60mm)	60mm; SS1, A1; SP4, steel	60mm flat, nose toward +x,SP4S flat, along x
1/15/2010	20100115_	27.5(clutter);38(60mm)	60mm; SS1, A1; SP4, steel; SP4, A1	60mm flat, nose toward +x,SP4S flat, along x, SP4A flat, along y
1/15/2010	20100115_	27.5(clutter);38(60mm)	60mm; SS1, A1; SP4, steel; SP4 A1; SP3 steel	60mm flat, nose toward +x,SP4S flat, along x, SP4A flat, along y; SP3S flat, along x
1/15/2010	20100115_	27.5(clutter);38(60mm); 63(105mm)	60mm; 105mm; SS1, A1; SP4, steel; SP4 A1; SP3 steel	60mm/105mm flat, nose toward +x,SP4S flat, along x, SP4A flat, along y; SP3S flat, along x
1/15/2010	20100115_	27.5(clutter);38(60mm); 63(105mm)	60mm; 105mm; SS1, A1; SP4, steel; SP4 A1	60mm/105mm flat, nose toward +x,SP4S flat, along x, SP4A flat, along y
1/15/2010	20100115_	27.5(clutter);38(60mm); 63(105mm)	60mm; 105mm; SS1, A1; SP4, steel	60mm/105mm flat, nose toward +x,SP4S flat, along x
1/15/2010	20100115_	27.5(clutter);38(60mm); 63(105mm)	60mm; 105mm; SS1, A1	60mm/105mm flat, nose toward +x
1/15/2010	20100115_	38(60mm); 63(105mm)	60mm; 105mm	60mm/105mm flat, nose toward +x

Table 8: Sample data cases from TEMTADS multiobject data set, January, 2010.

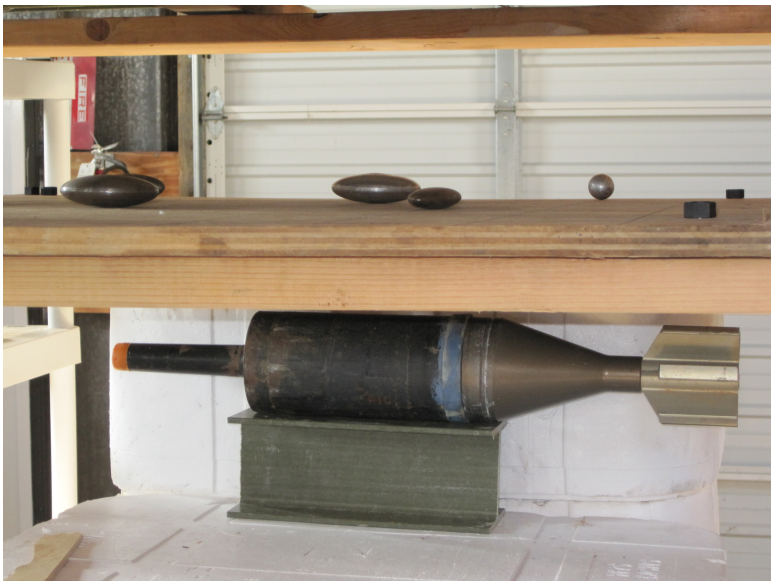

Figure 19: Sample setup for TEMTADS multitarget data collection.

5.2 MetalMapper Data and Results

To date, there is no good set of data from the MetalMapper over multiple targets. As a substitute, we constructed a set of multitarget data from single target data via superposition. This data comes from test data that Dave George took while calibrating the MetalMapper. For this test, one of three targets:

1. 10cm diam sphere
2. 13cm piece of rebar
3. 21cm diameter copper ring

were placed in one of five positions under the MetalMapper (see Fig. 21).

In the magnetoquasistatic (MQS) regime, the data can be superposed without difficulty. Therefore, multitarget test data was synthesized by adding up the data from different cases of targets in different quadrants. Table 9 shows the original data from which these blind tests were synthesized. These original data were superposed (added) in the following combinations (see Table 10) before being given to Dr. Fridon Shubitidze and Dr. Tomasz Grzegorczyk as a blind data set.

Using the multiple dipole Jacobian based gradient search method (see Sec. 4.2), Dr. Grzegorczyk was able to correctly identify all the targets in the semiblind data sets (see Figs. 22 and 23). The results for each case are computed in under one

Case #	Trg#1	Trg#2	Trg#3	Trg#4	Trg#5	Trg#6
117	60mm (0,-40,-38)	x	x	x	x	x
118	60mm (0,-40,-38)	SS1 (21,22,-26)	x	x	x	x
119	60mm (0,-38,-38)	SS1 (20,20,-26)	SP4S (-20,-20,-28)	x	x	x
120	60mm (0,-37,-40)	SS1 (22,21,-25)	SP4S (-19,-19,-29)	SP4A (-14,28,-30)	x	x
121	60mm (0,-34,-32)	SS1 (18,23,-26)	SP4S (-19,-20,-31)	SP4A (-24,19,-33)	SP4S (30,-8,-28)	
122	60mm (0,-35,-37)	SS1 (23,21,-21)	SP4S (-10,-17,-33)	SP4A (-24,-19,-26)	SP4S (30,-8,-28)	105 mm (0,37, -57)
123	60mm (0,-35,-37)	SS1 (23,24,-21)	SP4S (-12,-10,-33)	SP4A (-28,-30,-24)	x	105 mm (0,41, -57)
124	60mm (0,-37,-38)	SS1 (20,19,-19)	SP4S (-19,-20,-29)	x	x	105 mm (0,36, -57)
125	60mm (0,-38,-39)	SS1 (22,20,-23)		x	x	105 mm (0,38, -58)
126	60mm (0,-38,-39)	x		x	x	105 mm (0,41, -60)

Figure 20: Blind inversion results from Dr. Shubitidze using the combined JD and ONVMS methods. All targets correctly identified and positions are within the size of the target.

minute if the number of targets, N, is known. Finding N for this method, however, still requires an expert's interpretation of the polarizabilities assuming different N.

Using the combined JD and ONVMS methods, each of the 1-5 targets was also correctly identified for this blind set of MetalMapper data (see Fig. 24). These results take longer (10's of minutes for each case) to compute, but are aided by an estimate for N provided by the JD method.

5.3 MPV2 Data

MPV2 data was collected recently at CRREL in Hanover, NH in support of several SERDP project and with many goals in mind:

- Collect data over small targets at several depths including greater than 11 times the diameter (in support of MR-2106)
- Collect data over 2 and 3 target scenarios both small and larger targets in several combinations (in support of MR-2106 and MR-1664)
- Collect data over deep, larger targets

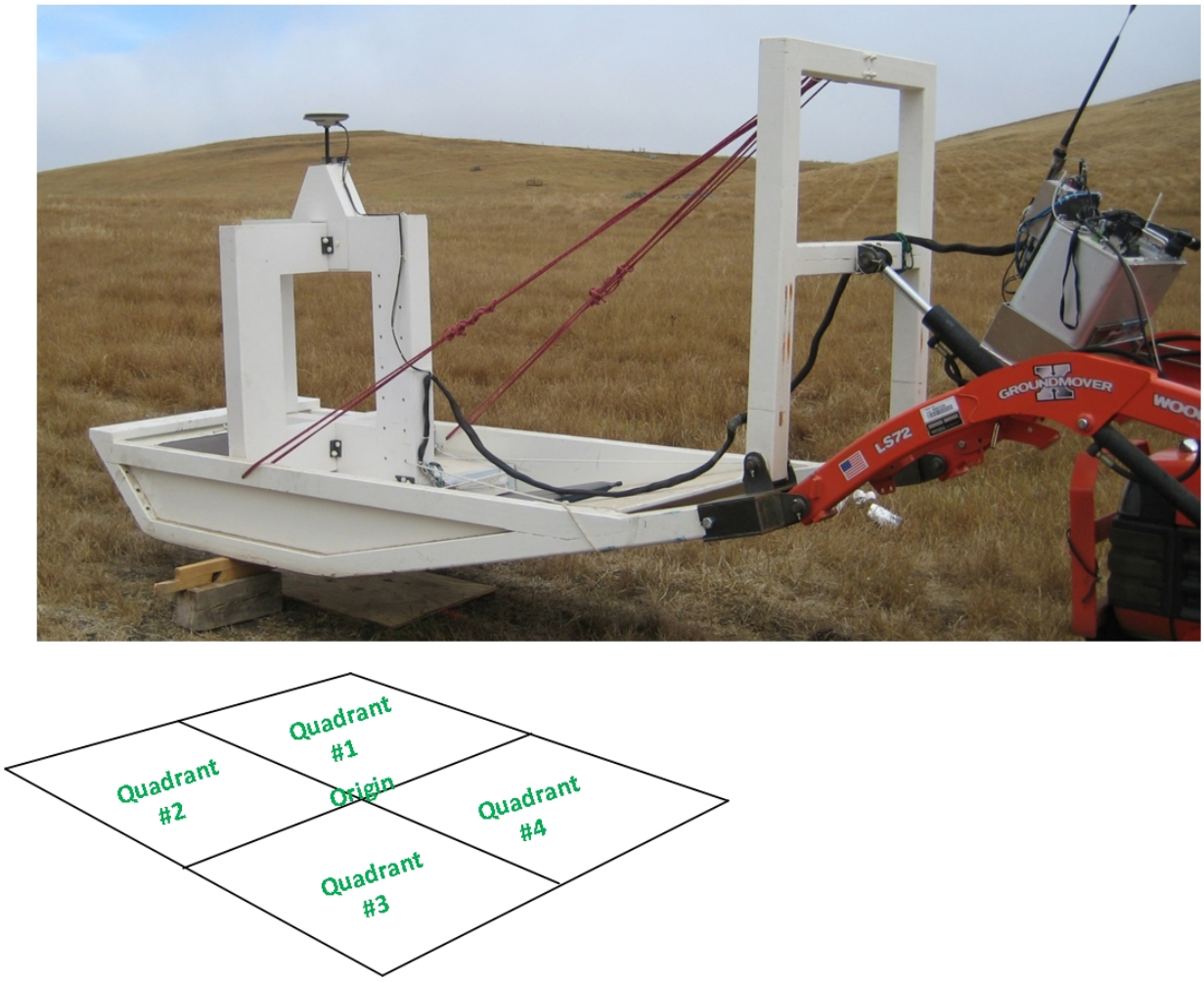

Figure 21: MetalMapper test setup with one of three targets in one of five positions. Blind multi-target test data synthesized by superposing different data cases.

- Collect data of small and large targets with a clutter layer between the targets and the MPV2 (in support of MR-2106 and MR-1664 and MR-1005)
- To carefully characterize the beacon positioning system accuracy in terms of both position and orientation
- To investigate the integration time of the DAQ window of the MPV2 in order to optimize the data acquisition protocol (in support of MR-1005 and future MPV2 projects)
- To collect some data used for blind tests for our recent algorithms as applied to handheld sensors

File #	target	depth to bottom of target	orientation	quadrant
2	sphere	35cm	N/A	1
3	ring	35cm	horizontal(H)	1
4	ring	35cm	vertical(V)- 0deg	1
5	rebar	35cm	horizontal - 0deg	1
6	sphere	35cm	N/A	2
7	ring	35cm	H	2
8	ring	35cm	V - 0deg	2
9	rebar	35cm	H - 0deg	2
10	sphere	35cm	N/A	3
11	ring	35cm	V - 0deg	3
12	ring	35cm	H - 0deg	3
13	rebar	35cm	H - 0deg	3
14	sphere	35cm	N/A	4
15	ring	35cm	H - 0deg	4
16	ring	35cm	V - 0deg	4
17	rebar	35cm	H - 0deg	4
18	sphere	35cm	N/A	0
19	ring	35cm	H - 0deg	0
20	ring	35cm	V - 0deg	0
21	rebar	35cm	H - 0deg	0

Table 9: Original MetalMapper calibration data.

We collected this data in February 2011, and we believe our data set will fulfill all these stated goals above, but we have not had time to produce any results from this data set.

6 Conclusions to Date

SERDP project MR-1664 entitled "Isolating and Discriminating Overlapping Signatures in Cluttered Environments" is approximately halfway complete. We have developed two major methods of finding multiple targets in EMI data even when the targets are in close proximity. The multiple dipole Jacobian based gradient search method (see Sec. 4.2) finds multiple targets by assuming that each target exhibits a dipolar response. A gradient search algorithm then searches for these multiple sources. At this point, this method needs to know the number of targets in order to perform accurately. The JD method provides this estimate for N to either the Jacobian search method or the ONVMS method. The ONVMS method (see

blind test #	original file #'s
1	[18,2]
2	[13,2,7]
3	[4,7,13,14]
4	[9,21]
5	[16,3]
6	[19,10,6,5]
7	[8,21,17]
8	[15,11,9]
9	[5,8,10,15,20]

Table 10: MetalMapper blind test data configurations synthesized by superposing data cases from Table 9.

Case nb	Nb of targets	Targets id				
1	2	2	18	-	-	-
2	3	2	7	13	-	-
3	3	4	7	13	14	-
4	2	21	9	-	-	-
5	2	3	16	-	-	-
6	4	5	6	10	19	-
7	3	8	21	17	-	-
8	3	11	9	15	-	-
9	5	5	8	10	15	20

Figure 22: Results from using the multiple dipole Jacobian based gradient search method. Refer to Tables 9 and 10.

Sec. 4.3) searches for dipole like (but orthonormal) sources in the data without inversion difficulties arising from solving linear systems. Both of these methods are able to distinguish at least six different targets in EMI data from either the TEMTADS or MetalMapper instruments. The combined JD and ONVMS method (together with expert guidance) performed very well at the Camp Butner demonstration site at the Partners 2010 symposium. We still plan to investigate Particle Filtering techniques as part of the remainder of this project.

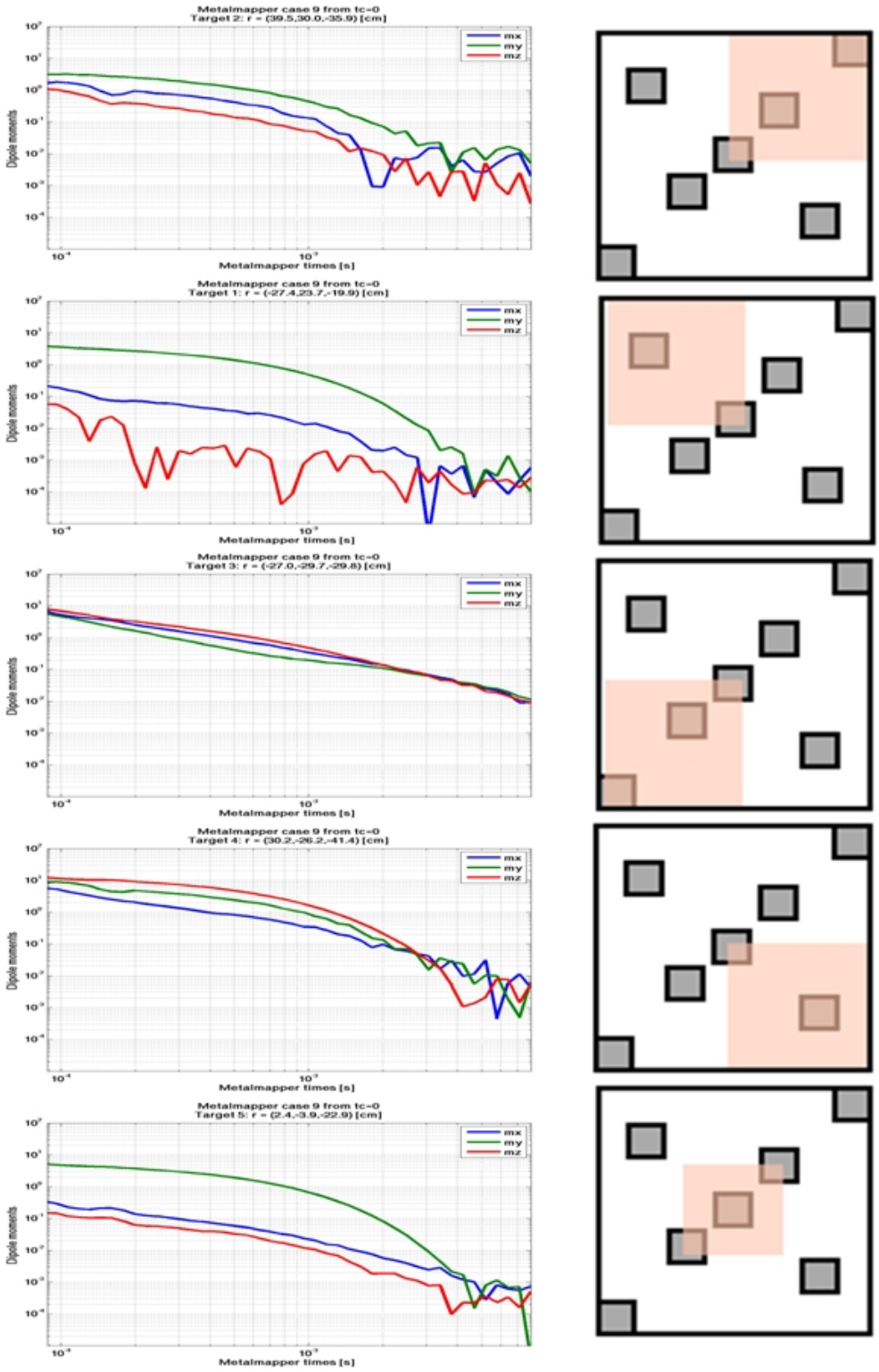

Figure 23: Polarizabilities extracted for bind case 9 using the Jacobian multiple dipole search method. Refer to Tables 9 and 10.

Case #	Object 1/ Location (cm)	Object 2/ Location (cm)	Object 3/ Location (cm)	Object 4/ Location (cm)	Object 5/ Location (cm)
1	Sphere / (26, 28, -37)	Sphere / (0,0, -35)	N/A	N/A	N/A
2	Sphere / (26, 28, -37)	Ring / (-26, 21, -28)	Rebar/ (-27, -28, -38)	N/A	N/A
3	Ring / (31, 28, -29)	Ring/ (-26, 21, -42)	Rebar / (-27, -28,-38)	Sphere/ (29, -26,-35)	N/A
4	Rebar/ (-28, 24, -38)	Rebar/ (0,0,-36)	N/A	N/A	N/A
5	Ring/ (26, 28, -41.5)	Ring/ (29,-27,-29)	N/A	N/A	N/A
6	Rebar/ (28,23,-38)	Sphere/ (-28, 24,-35)	Sphere/ (-26, -30, -35)	Ring/ (0,0,-40)	N/A
7	Ring/ (-30,23,-28)	Rebar/ (25,-32,37)	Rebar/ (0,0,-36)	N/A	N/A
8	Rebar/ (-28,24,-38)	Ring/ (-25,-30,-28.5)	Ring/ (29,-27,-43)	N/A	N/A
9	Rebar/ (28, 23, -38)	Ring/ (-30,23, -28)	Sphere/ (-26,-30, -30)	Ring/ (29,-27,-29)	Ring (0,0,-27)

Figure 24: Inversion results from using the combined JD and ONVMS methods. Refer to Tables 9 and 10.

A Appendices – Supporting Data

A.1 MPV Single Target Blind Test Results

We collected data using the MPV1 instrument over several single target cases as a blind test for our models. During the data collection, we employed the laser positioning system to locate our data though we used a grid as a rough guide when we moved the MPV instrument itself. We took data at two heights, separated by 10 cm or two blue board thicknesses. At each height and after acquiring background data, we took a total of 17 measurement in a four by four grid followed by a single shot located precisely on our grid. We used this last data point to define a global coordinate system for each set of 17 data points. The true locations and orientation of the five targets are given in Table 11. These results are very encouraging for single target cases even considering only 5 data shots (=75 data points) from the MPV. Sample results, presented at Partners 2007, are given in Fig. 25.

Target	ID	x_0 (cm)	y_0 (cm)	z_0 (cm)	ϕ (°)	dip (°)
1	81-mm	−23.26	22.5	56.16	0	−18.3
2	105-mm	−20.26	22.5	69.14	180	−18.6
3	BLU26	0.00	22.5	43.21	0	0.0
4	57-mm	5.22	22.5	51.45	180	306.6
5	60-mm	0.00	22.5	54.50	0	0.0

Table 11: Correct answers for the blind-test data runs.

Target	ID	x_0 (cm)	y_0 (cm)	z_0 (cm)	ϕ (°)	dip (°)
1	81-mm	-21.2	23.6	56.56	0	−2
2	105-mm	- 6.0	23.7	67.57	170	−20.8
3	BLU26	0.25	21.8	47.55	*0	*180
4	57-mm	0.75	21.6	58.19	0	320.4
5	60-mm	0.67	19.3	54.02	*3	0

Table 12: NSMC model inversion results for position and orientation for blind test data. Numbers with an asterisk are arbitrary due to BOR considerations.

A.2 Previous Multiple Target Inversion Results

Though we would not use the GEM-3 for the research proposed here, our prior work in this area involves GEM-3 data.

We acquired data using the GEM-3 instrument in 2005 over 9 sets of targets in the CRREL test plots. In each test hole, we emplaced either 1 UXO and 1 piece of clutter, or 2 UXOs. We then acquired data at two elevations over each test hole and used these data in a blind test. Sample data from one of the test holes is shown in Fig. 26. As can be seen from the picture, it is not at all clear by eye how

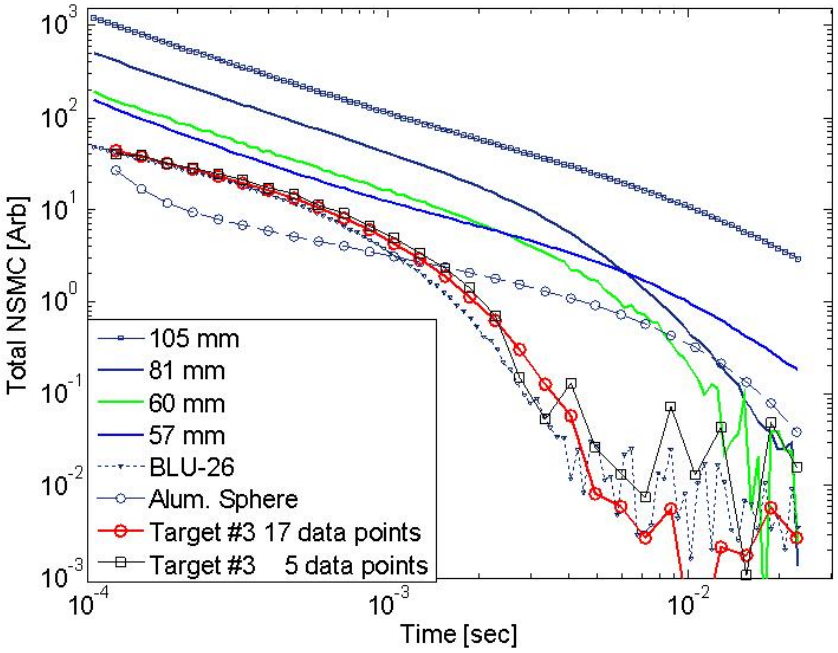

Figure 25: NSMC model comparison to library for blind test #3.

many targets are present in the data much less where they are located. The NSMC model was used to simultaneously invert for the positions, orientations and Q (or the total NSMC) for each of these test holes. Results are shown in Fig. 27. The NSMC algorithm was able to discriminate between targets in close proximity in some cases, but in others, the results were less clear.

While encouraging this study provides an excellent example of the problems faced when signals from objects overlap [11, 14, 68]. These problems include positional uncertainties, scalar data, and sensor limitations. The research we propose here aims to overcome these limitations with clutter mitigation techniques, an N-target locator, and more diverse, higher quality data.

A.2.a GEM-3 Data over 2 UXO

Data were collected on a 7x7 grid at two heights above each test hole. The NSMC was then used in an iterative fashion in an attempt to discriminate both UXO simultaneously.

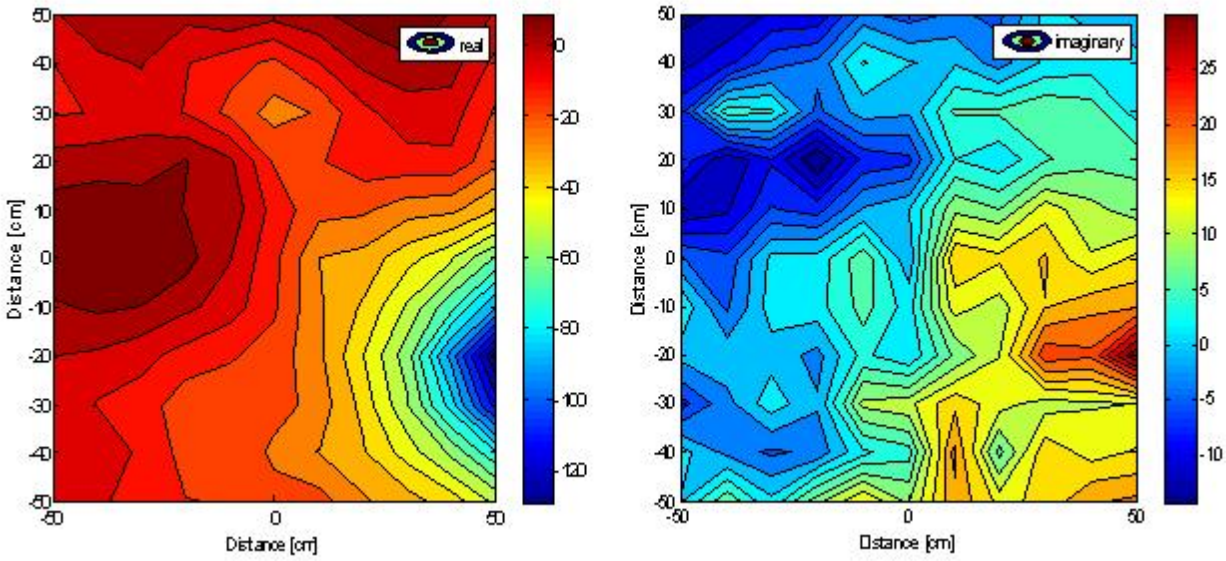

Figure 26: GEM-3 data acquired over 2 buried targets.

A.2.b Projection of GEM-3 Data over 1 UXO Obscured by Clutter

Data projection involves using the data from mono-static or multi-static instruments to achieve the same purpose as that for bistatic instruments, that is, to use data at lower elevations (closer to clutter) to provide estimates on what data would look like if acquired at higher elevations (farther from clutter). An early attempt at a data projection technique for GEM-3 data is described here.

We acquired data from a 105mm UXO (Fig. 28) which was obscured by the clutter layer affixed to a plywood substrate as shown in Fig. 29. The clutter layer was situated 5cm above the upmost part of the UXO, and GEM-3 measurements were taken at 2 heights: 15cm and 20 cm above the upmost part of the UXO respectively. The H_z at 90Hz from the GEM-3 is shown at these two height in Fig. 30 (top subfigures). Using our preliminary upward projection technique, we were able to use these data at lower heights to estimate data as if acquired at higher elevations (in this case 25cm and 30cm above the UXO). These projected in Fig. 30 (bottom subfigures) show the diminished influence of the clutter layer as a function of height. Note that this clutter layer is an extreme case (to begin with) and reacts almost as a sheet of dispersed clutter, which has a different power law than discrete targets [69].

The decay of the projected data for both the UXO+clutter case and the clutter only case both approach the same power law. This suggests that the higher up

Tasks #	Inverted targets		Ground truth	
	Object #1	Object #2	Object #1	Object#2
1		Clutter	Correct	Correct
2		Clutter	Correct	Correct
3		Clutter	Incorrect	Correct
4		Clutter	Incorrect	Correct
5			Correct	Correct
6			Correct	Incorrect
7			Incorrect	\ Correct
8		An aluminum plate ??	Correct	Incorrect
9			Incorrect	Correct

Figure 27: GEM-3 data inversion results from Partners poster 2006.

the data is projected, the less the influence the clutter has until only the EMI response from the UXO is non-negligible. This effect may be exploited for use in discrimination and needs further research.

B List of Scientific/Technical Publications

Publications produced in whole or part with funds from this project are [1, 70–79].

C Other Supporting Materials

References

[1] F. Shubitidze, B. Barrowes, I. Shamatava, and K. O'Neill. Multiple subsurface targets localization from next-generation EMI sensor data using MUSIC algorithm. Proc. IEEE Int. Geosci. Remote Sensing Symp. (IGARSS), 2010. ii, 1, 3, 57

Figure 28: 105mm UXO under clutter layer.

Figure 29: Dense clutter layer affixed to plywood substrate.

[2] Fridon Shubitidze, Irma Shamatava, Alex Bijamov, Ben Barrowes, and Kevin O'Neill. Camp butner uxo data inversion and classification using advanced emi models. SERDP-MR-1572. 1

[3] F. Shubitidze, K. O'Neill, K. Sun, and I. Shamatava. Interaction between highly conducting and permeable metallic objects in the EMI frequency range. Annual Review of Progress in Applied Computational Electromagnetics, pages 625 – 631, 2003. 2

[4] F. Shubitidze, K. O'Neill, I. Shamatava, K. Sun, and K.D. Paulsen. Analysis of EMI scattering to support UXO discrimination: Heterogeneous and multi objects. Proceedings of SPIE - The International Society for Optical Engineering, 5089(2):928 – 939, 2003. ISSN 0277-786X. 2, 33, 34

[5] Wei Hu, Stacy L. Tantum, and Leslie M. Collins. EMI-based classification of multiple closely spaced subsurface objects via independent component analysis. IEEE Transactions on Geoscience and Remote Sensing, 42(11): 2544 – 2554, 2004. ISSN 0196-2892. 2, 10

[6] Chandra S. Throckmorton, Stacy L. Tantum, Yingyi Tan, and Leslie M. Collins. Independent component analysis for UXO detection in highly cluttered environments. Journal of Applied Geophysics, 61(3-4):304 – 317, 2007. ISSN 0926-9851. 2

[7] Ian T. McMichael and Carl V. Nelson. Investigation of the electromagnetic induction spatial response of two closely spaced targets. volume 5089, pages 894 – 903, Orlando, FL, United States, 2003. 2, 10

[8] F. Shubitidze, K. O'Neill, S.A. Haider, Keli Sun, and K.D. Paulsen. Application of the method of auxiliary sources to the wide-band electromagnetic induction problem. IEEE Transactions on Geoscience and Remote Sensing, 40(4):928 – 42, 2002/04/. ISSN 0196-2892. 2

[9] K. O'Neill, K. Sun, C.C. Chen, F. Shubitidze, and K.D. Paulsen. Combining GPR and EMI Data for Discrimination of Multiple Subsurface Metallic Objects. volume 7, pages 4157 – 4159, Toulouse, France, 2003. 2, 10

[10] K. Sun, K. O'Neill, C.-C. Chen, H. S. Youn, F. Shubitidze, I. Shamatava, , and K.D. Paulsen. Highly contaminated UXO sites: combination of GPR and EMI for discrimination of clustered scatterers. SAGEEP, 2005. 2, 10

[11] F. Shubitidze, K. O'Neill, I. Shamatava, K. Sun, , and K. D. Paulsen. Total magnetic charge for fast screening of highly contaminated UXO sites. In proceedings of 2005 IEEE international symposium on Antennas and Propagation and USNC/CN/URSI North American Radio Science meeting, on CD, 2005. 2, 55

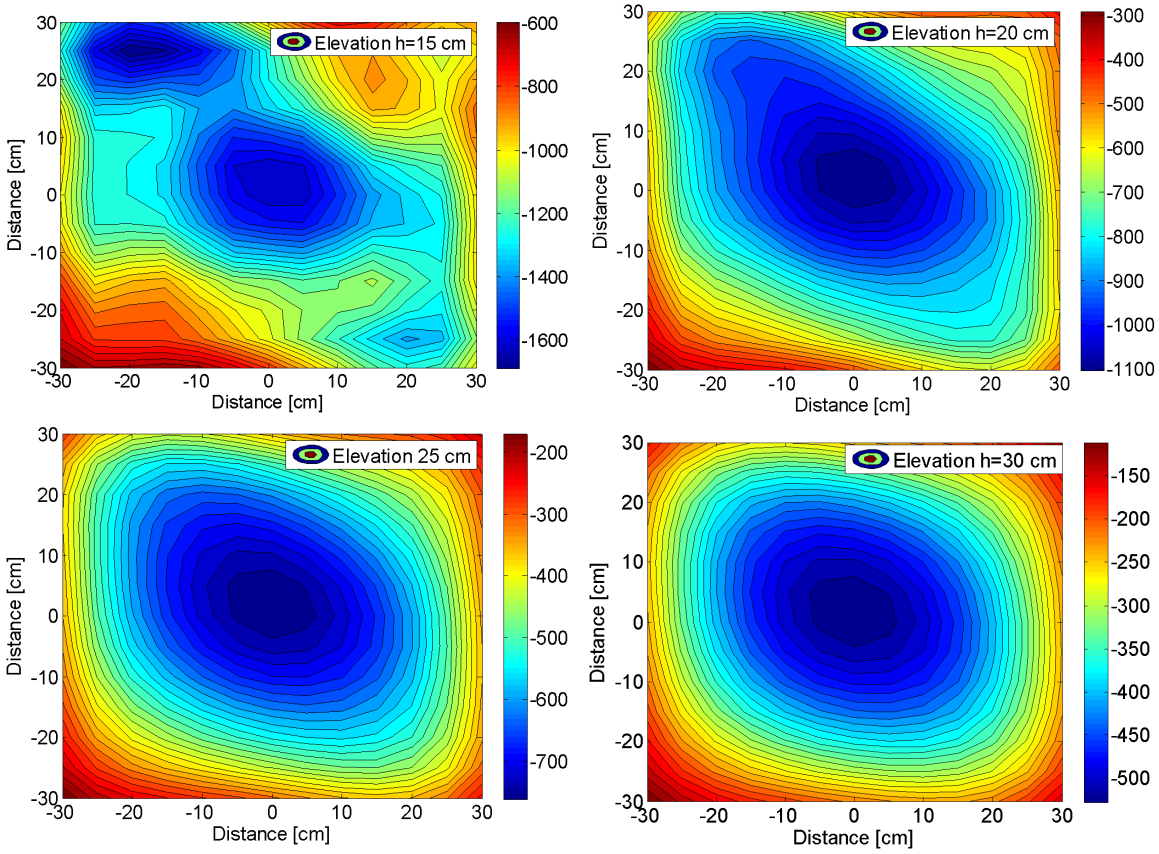

Figure 30: As the sensor is raised, the contribution of clutter to the overall EMI response is reduced compared to the response of the 105mm UXO.

[12] I. Shamatava, F. Shubitidze, C.C. Chen, H.S. Youn, K. O'Neill, and K. Sun. Potential benefits of combining EMI and GPR for enhanced UXO discrimination at highly contaminated sites. Proceedings of SPIE - The International Society for Optical Engineering, 5415(PART 2):1201 – 1210, 2004. ISSN 0277-786X. 2

[13] Leslie M. Collins, Yan Zhang, and Lawrence Carin. Model-based statistical sensor fusion for unexploded ordnance detection. volume 3, pages 1556 – 1559, Toronto, Ont., Canada, 2002. 2

[14] F. Shubitidze, B. Barrowes, and K. O'Neill. Normalized surface magnetic charge for UXO discrimination: multiple objects. SERDP Partners Symposium, November 2006. Poster. 3, 55

[15] K. O'Neill, S.A. Haider, S. Geimer, and K.D. Paulsen. Effects of the ground surface on polarimetric features of broadband radar scattering from subsurface metallic objects. IEEE Trans. on Geosci. Remote Sens., 39(6): 1556–1565, June 2001. 10

[16] Chi-Chih Chen, Matthew B. Higgins, Kevin O'Neill, and Richard Detsch. Ultrawide-bandwidth fully-polarimetric ground penetrating radar classification of subsurface unexploded ordnance. IEEE Trans. Geosci. Remote Sens., 39:1221–1230, June 2001. 10

[17] C. E. Baum. Detection and Identification of Visually Obscured Targets. Taylor & Francis, Philadelphia, 1999. 10

[18] John David Jackson. Classical Electrodynamics. Wiley, New York, 2nd edition, 1975. 10, 13, 14

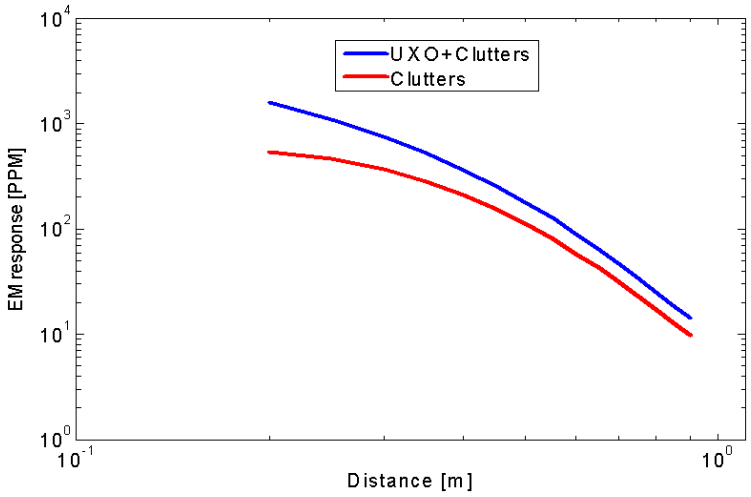

Figure 31: Projected data as a function of elevation at the center of the measurement grid.

[19] T. H. Bell, B. J. Barrow, and J. T. Miller. Subsurface discrimination using electromagnetic induction sensors. IEEE Trans. on Geoscience and Remote Sensing, 39(6):1286–1293, June 2001. 10

[20] Yan Zhang, L. Collins, Haitao Yu, C.E. Baum, and L. Carin. Sensing of unexploded ordnance with magnetometer and induction data: theory and signal processing. IEEE Transactions on Geoscience and Remote Sensing, 41(5): 1005 – 15, 2003/05/. ISSN 0196-2892. 10, 33, 34

[21] C. O. Ao, H. Braunisch, K. O'Neill, and J. A. Kong. Quasi-magnetostatic solution for a conducting and permeable spheroid with arbitrary excitation. IEEE Trans. on Geoscience and Remote Sensing, 40(4):887–897, April 2002. 10

[22] Benjamin E. Barrowes, Kevin O'Neill, Tomasz M. Grzegorczyk, Xudong Chen, and Jin A. Kong. Broadband analytical magnetoquasistatic electromagnetic induction solution for a conducting and permeable spheroid. IEEE Trans. on Geoscience and Remote Sensing, 42(11):2479–2489, November 2004. 10

[23] Tomasz M. Grzegorczyk, Beijia Zhang, Jin Au Kong, Benjamin E. Barrowes, and Kevin O'Neill. Electromagnetic induction from highly permeable and conductive ellipsoids under arbitrary excitation - application to the detection of unexploded ordnances. IEEE Trans. on Geoscience and Remote Sensing, 46(4):1164–1176, April 2008. 10

[24] F. Shubitidze, K. O'Neill, B.E. Barrowes, I. Shamatava, J.P. Fernandez, K. Sun, and K.D. Paulsen. Application of the normalized surface magnetic charge model to UXO discrimination in cases with overlapping signals. Journal of Applied Geophysics, 61(3-4):292 – 303, 2007. ISSN 0926-9851. 10, 33, 34, 38

[25] C. D. Moss, T. M. Grzegorczyk, K. O'Neill, and J. A. Kong. A hybrid time domain model of electromagnetic induction from conducting, permeable targets. IEEE Trans. on Geoscience and Remote Sensing, 44(10):2916–2926, October 2006. 10

[26] S. L. Tantum and L. M. Collins. A comparison of algorithms for subsurface target detection and identification using time-domain electromagnetic induction data. IEEE Trans. on Geosci. Remote Sens., 2001. 10

[27] Xudong Chen, K. O'Neill, T.M. Grzegorczyk, and Jin Au Kong. Spheroidal mode approach for the characterization of metallic objects using electromagnetic induction. IEEE Transactions on Geoscience and Remote Sensing, 45(3):697 – 706, 2007/03/. ISSN 0196-2892. 10

[28] Fridon Shubitidze, Juan Pablo Fernández, Benjamin E. Barrowes, Irma Shamatava, and Kevin O'Neill. Normalized Surface Magnetic Source model applied to Camp Sibert data: Discrimination studies. In Applied Computational Electromagnetics Symposium (ACES), Monterey, CA, Mar. 2009. 10

[29] Juan Pablo Fernández, Fridon Shubitidze, Irma Shamatava, Benjamin E. Barrowes, and Kevin O'Neill. Realistic subsurface anomaly discrimination using electromagnetic induction and an svm classifier. Applied Computational Electromagnetics Journal. 10

[30] Chandra S. Throckmorton, Stacy L. Tantum, Yingyi Tan, and Leslie M. Collins. Independent component analysis for UXO detection in highly cluttered environments. Journal of Applied Geophysics, 61(3-4):304–317, 2007. 11

[31] Lin-Ping Song, Douglas W. Oldenburg, Leonard R. Pasion, and Stephen D. Billings. Transient electromagnetic inversion for multiple targets. SPIE Proceedings, 7303, May 2009. 11, 15

[32] A. J. Devaney. Time reversal imaging of obscured targets from multistatic data. 53(5):1600–1610, May 2005. doi: 10.1109/TAP.2005.846723. 11

[33] F. Shubitidze, B. Barrowes, I.Shamatava, and K. O'Neill. Multiple subsurface target localization from next generation EMI sensor data using MUSIC algorithm. IGARSS, 2010. 11

[34] Yu Zhong and Xudong Chen. MUSIC imaging and electromagnetic inverse scattering of multiply scattering small anisotropic spheres. 55(12):3542–3549, December 2007. doi: 10.1109/TAP.2007.910488. 11

[35] Tomasz M. Grzegorczyk, Benjamin Barrowes, Fridon Shubitidze, J. P. Fernandez, Irma Shamatava, and Kevin O'Neill. Kalman filters applied to the detection of unexploded ordnance. In Proc. of SPIE, Detection and Sensing of Mines, Explosive Objects, and Obscured Targets, volume 7664, 2010. doi: 10.1117/12.848564. Orlando, FL. 11

[36] Tomasz M. Grzegorczyk, Benjamin Barrowes, Fridon Shubitidze, J. P. Fernandez, Irma Shamatava, and Kevin O'Neill. Detection of multiple subsurface metallic targets using EMI data. In Proc. of SPIE, Detection and Sensing of Mines, Explosive Objects, and Obscured Targets, volume 73030T, 2009. Orlando, FL. 11

[37] H. H. Nelson and J. R. McDonald. Multi-sensor towed array detection system (mtads) for uxo detection. IEEE Trans. on Geosci. Remote Sens., 39(6):1139–1145, June 2001. 11

[38] H. H. Nelson, D. A. Steinhurst, B. Barrow, T. Bell, N. Khadar, B. SanFilipo, and I. J. Won. Enhanced UXO discrimination using frequency-domain electromagnetic induction. Final report to the ESTCP program office (DOD) Arlington VA for project MM-0601, Naval Research Laboratory, 2007. URL http://oai.dtic.mil/oai/oai?&verb=getRecord&metadataPrefix=html&identifier=ADA469893. Accession Number : ADA469893. 11

[39] David C. George and Joan L. George. Data report: Tests of MPV at Vicksburg, February 26 to March 2, 2007. Technical Note 2007-2. Grand Junction, CO: G&G Sciences Inc. (http://www.ggsciences.com), 2007. 11, 13

[40] Julius Adams Stratton. Electromagnetic Theory. McGraw-Hill, New York, 1941. 13

[41] Fridon Shubitidze, Kevin ONeill, Shah A. Haider, Keli Sun, and Keith D. Paulsen. Application of the method of auxiliary sources to the wide-band electromagnetic induction problem. IEEE Trans. on Geosci. Remote Sens., 40(4):928–942, April 2002. 14

[42] F. Shubitidze, K. ONeill, I. Shamatava, and K. Sun. Coupling between highly conducting and permeable metallic objects in the emi frequency range. Applied computational electromagnetic society Journal, pages 139–148, March 2004. 14

[43] Henning Braunisch, Chi O. Ao, Kevin ONeill, and Jin A. Kong. Magnetoquasistatic response of a distribution of small conducting and permeable objects. In IEEE 2000 International Geoscience and Remote Sensing Symposium, 2000. 14

[44] F. Shubitidze, K. O'Neill, I. Shamatava, K. Sun, and K. D. Paulsen. A standardized excitation approach for classification of buried UXO. In IEEE 2000 International Geoscience and Remote Sensing Symposium, volume 7, pages 4905–4908, 2004. 15

[45] Jonathan Miller. Classification using electromagnetic induction sensors. In UXO Forum, Orlando, FL, 24-27 August 2009. 15

[46] . We acknowledge the work of Dr. Dan Steinhurst of Nova Research Inc. in acquiring TEMTADS data. 18

[47] . We acknowledge the work of Drs. Gregory Schultz, Sam Segal, and Irma Shamatava of Sky Research Inc. in acquiring MPV data. 18

[48] . We acknowledge the private communication with Dr. James Kingdon of SAIC for the validation of single target TEMTADS inversion results. 23

[49] Fridon Shubitidze, David Karkashadze, Juan Pablo Fernandez, Benjamin E. Barrowes, Kevin O'Neill, Tomasz M. Grzegorczyk, and Irma Shamatava. Applying a volume dipole distribution model to next-generation sensor data for multi-object data inversion and discrimination. Proc. of SPIE, page 766407, 2010. 23

[50] W. P. Delaney and D. Etter. Report of the defense science board task force on unexploded ordnance. Final tech. rep. a079914, Defense Sci. Board, Washington DC, 2003. 32, 33, 34

[51] J.T. Miller, T.H. Bell, J. Soukup, and D. Keiswetter. Simple phenomenological models for wideband frequency-domain electromagnetic induction. IEEE Transactions on Geoscience and Remote Sensing, 39(6):1294 – 1298, 2001. ISSN 0196-2892. 33, 34

[52] L. R. Pasion and D. W. Oldenburg. A discrimination algorithm for UXO using time domain electromagnetics. J. Engg & Envir. Geophys, Vol. 20:pp91–102, 2001. 33, 34

[53] J. T. Smith, H. F. Morrison, and A. Becker. Resolution depths for some transmitter-receiver configurations. IEEE Trans on. GeoSc. And Remote Sen., 42(6):1215–1221, 2004. 33, 34

[54] Bruce J. Barrow and H. H. Nelson. Model-based characterization of electromagnetic induction signatures obtained with the MTADS electromagnetic array. IEEE Trans. Geosci. Remote Sens., 39:1279–1285, June 2001. 33

[55] K. Sun, K. O'Neill, F. Shubitidze, I. Shamatava, and K.D. Paulsen. Fast data-derived fundamental spheroidal excitation models with application to UXO identification. Proceedings of SPIE - The International Society for Optical Engineering, 5415(PART 2):855 – 865, 2004. ISSN 0277-786X. 33, 34

[56] F. Shubitidze, K. O'Neill, I. Shamatava, K. Sun, and K.D. Paulsen. A simple magnetic charge model for classification of multiple buried metallic objects in cases with overlapping signals. SAGEEP, 2005. 33

[57] Fridon Shubitidze, Kevin O'Neill, Irma Shamatava, Keli Sun, and Keith Paulsen. Combined differential evolution and surface magnetic charge model algorithm for discrimination of UXO from non-UXO items: Simple and general inversions. Proceedings of SPIE - The International Society for Optical Engineering, 5794(PART I):346 – 357, 2005. ISSN 0277-786X. 33

[58] Fridon Shubitidze, Kevin O'Neill, Irma Shamatava, Keli Sun, and Keith D. Paulsen. Fast and accurate calculation of physically complete EMI response by a heterogeneous metallic object. IEEE Transactions on Geoscience and Remote Sensing, 43(8):1736 – 1750, 2005. ISSN 0196-2892. 33

[59] Lin-Ping Song, Fridon Shubitidze, Leonard R. Pasion, Douglas W. Oldenburg, and Stephen D. Billings. Computing transient electromagnetic response of a metallic object with a spheroidal excitation approach. Geoscience and Remote Sensing, IEEE Transactions Letter, 2008. 33

[60] F. Shubitidze, K. O'Neill, I. Shamatava, K. Sun, and K.D. Paulsen. Use of standardized source sets for enhanced EMI classification of buried heterogeneous objects. Proceedings of SPIE - The International Society for Optical Engineering, 5415(PART 1):263 – 274, 2004. ISSN 0277-786X. 33

[61] H. Braunisch, C. O. Ao, K. O'Neill, and J. A. Kong. Magnetoquasistatic response of conducting and permeable spheroid under axial excitation. IEEE Trans. on Geoscience and Remote Sensing, 39(12):2689–2701, December 2001. 33

[62] C. O. Ao, H. Braunisch, K. O'Neill, , and J. A. Kong. Quasi-magnetostatic solution for a conducting and permeable spheroid with arbitrary excitation. IEEE Trans. on Geoscience and Remote Sensing, 40(4):887–97, April 2002. 33

[63] B. E. Barrowes, K. O'Neill, T. M. Grzegorczyk, X. Chen, and J. A. Kong. Broadband analytical magnetoquasistatic electromagnetic induction solution for a conducting and permeable spheroid. IEEE Trans. on Geoscience and Remote Sensing, 42(11):2479–2489, 2004. 33

[64] T.H. Bell, B.J. Barrow, and J.T. Miller. Subsurface discrimination using electromagnetic induction sensors. IEEE Trans. on Geoscience and Remote Sensing, 39(6):1286 – 1293, June 2001. 33

[65] Rainer Storn and Kenneth Price. Differential evolution - a simple and efficient adaptive scheme for global optimization over continuous spaces. Technical Report TR-95-012, Berkeley, CA, 1995. 34, 35, 43

[66] R. Storn. System design by constant adaptation and differential evolution. IEEE Trans. Evol. Comput., 1999. 34, 35, 43

[67] J. F. Cardoso and A. Souloumiac. Jacobi angles for simultaneous diagonalization. SIAM Journal of Matrix Analysis and Applications, 17(1):161–164, 1996. 35, 40

[68] F. Shubitidze, B. Barrowes, J. P. Fernández, Irma Shamatava, and K. O'Neill. NSMC for UXO discrimination in cases with overlapping signatures. SPIE, 2007. 55

[69] K. O'Neill, Keli Sun, F. Shubitidze, I. Shamatava, and K.D. Paulsen. Accounting for the effects of widespread discrete clutter in subsurface EMI remote sensing of metallic objects. IEEE Transactions on Geoscience and Remote Sensing, 44(1):32 – 46, 2006. ISSN 0196-2892. 56

[70] Ben Barrowes, Tomasz Grzegorczyk, Fridon Shubitidze, Pablo Fernandez, and Kevin O'Neill. Techniques in electromagnetic induction for discriminating multiple targets. Memphis, TN, Nov 18 2009. USACE Research and Development Conference. 57

[71] Fridon Shubitidze, Juan Pablo Fernandez, Irma Shamatava, Leonard R. Pasion, Benjamin E. Barrowes, and Kevin O'Neill. Application of the normalized surface magnetic source model to a blind unexploded ordnance discrimination test. Applied Computational Electromagnetics Society Journal, 25(1):89 – 98, 2010. ISSN 10544887. 57

[72] Fridon Shubitidze, Juan Pablo Fernandez, Irma Shamatava, Benjamin E. Barrowes, and Kevin O'Neill. Realistic subsurface anomaly discrimination using electromagnetic induction and an svm classifier. Eurasip Journal on Advances in Signal Processing, 2010, 2010. ISSN 16876172. URL http://dx.doi.org/10.1155/2010/305890. 57

[73] J. P. Fernandez, B. Barrowes, A. Bijamov, T. Grzegorczyk, K. O'Neill, I. Shamatava, and F. Shubitidze. Combining electromagnetic induction and automated classification in a uxo discrimination blind test. Detection and Sensing of Mines, Explosive Objects, and Obscured Targets Xv, 7664, 2010. doi: 10.1117/12.850446. 57

[74] F. Shubitidze, J. P. Fernandez, B. E. Barrowes, K. O'Neill, I. Shamatava, and A. Bijamov. Comparison of the physically complete model with a simple dipole model for uxo detection and discrimination. Detection and Sensing of Mines, Explosive Objects, and Obscured Targets Xv, 7664, 2010. doi: 10.1117/12.850654. 57

[75] T. M. Grzegorczyk, B. Barrowes, F. Shubitidze, J. P. Fernandez, I. Shamatava, and K. O'Neill. Kalman filters applied to the detection of unexploded ordnance. Detection and Sensing of Mines, Explosive Objects, and Obscured Targets Xv, 7664, 2010. doi: 10.1117/12.848564. 57

[76] K. O'Neill, B. E. Barrowes, F. Shubitidze, J. P. Fernandez, T. M. Grzegorczyk, and I. Shamatava. Upward continuation of emi data for sensing of subsurface uxo in cluttered, multi-object cases. Detection and Sensing of Mines, Explosive Objects, and Obscured Targets Xv, 7664, 2010. doi: 10.1117/12.850441. 57

[77] I. Shamatava, F. Shubitidze, J. P. Fernandez, B. E. Barrowes, K. O'Neill, T. M. Grzegorczyk, and A. Bijamov. Slo blind data set inversion and classification using physically complete models. Detection and Sensing of Mines, Explosive Objects, and Obscured Targets Xv, 7664, 2010. doi: 10.1117/12.850621. 57

[78] T. M. Grzegorczyk, B. Barrowes, F. Shubitidze, J. P. Fernandez, and K. O'Neill. Simultaneous discrimination of multiple unexploded ordnance using electromagnetic induction sensors. IEEE Trans. on Geosci. Remote Sens., 2010. Accepted for publication. 57

[79] T.M. Grzegorczyk, B. Barrowes, F. Shubitidze, J.P. Fernandez, I. Shamatava, and K. ONeill. Detection of multiple subsurface metallic targets using emi data. In Proceedings of the SPIE - The International Society for Optical Engineering, volume 7303, 2009. 57